석 사 학 위 논 문
Master Thesis

광전 에너지 하베스팅 기반의 가스 센서 집적회로 설계

Self-Powered Gas Sensor IC Based on Photovoltaic Energy Harvesting

2019

Hung Phan

한 국 과 학 기 술 원

Korea Advanced Institute of Science and Technology

석 사 학 위 논 문

광전 에너지 하베스팅 기반의 가스 센서 집적회로 설계

2019

Hung Phan

한 국 과 학 기 술 원

전기및전자공학부

광전 에너지 하베스팅 기반의 가스 센서 집적회로 설계

Hung Phan

위 논문은 한국과학기술원 석사학위논문으로
학위논문 심사위원회의 심사를 통과하였음

2019년 6월 20일

심사위원장 제 민 규 (인)

심 사 위 원 류 승 탁 (인)

심 사 위 원 이 상 국 (인)

Self-Powered Gas Sensor IC Based on Photovoltaic Energy Harvesting

Hung Phan

Advisor: Professor Minkyu Je

A thesis submitted to the faculty of
Korea Advanced Institute of Science and Technology in
partial fulfillment of the requirements for the degree of
Master of Science in Electrical Engineering

Daejeon, Korea
June 24, 2019

Approved by

Minkyu Je
Professor of Electrical Engineering

The study was conducted in accordance with Code of Research Ethics[1)].

1) Declaration of Ethical Conduct in Research**:** I, as a graduate student of Korea Advanced Institute of Science and Technology, hereby declare that I have not committed any act that may damage the credibility of my research. This includes, but is not limited to, falsification, thesis written by someone else, distortion of research findings, and plagiarism. I confirm that my dissertation contains honest conclusions based on my own careful research under the guidance of my advisor.

MEE 20174562

Hung Phan. Self-Powered Gas Sensor IC Based on Photovoltaic Energy Harvesting. School of Electrical Engineering. 2019. 39+v pp. Advisor: Prof. Minkyu Je.

Abstract: A self-powered gas sensor integrated circuit (IC) suitable for wireless sensor nodes is designed in 0.18μm CMOS process. The novel idea of using the output of the photovoltaic (PV) cell covered by the gas-sensing film allows the proposed sensor system to have low power consumption and compact size. A dual-input shared-inductor boost converter is used to harvest energy efficiently from two PV cells instead of connecting these cells in parallel when the system is exposed to gases. This shows 17% improvement of conversion efficiency at 200ppm nitrogen dioxide gas concentration. Maximum end-to-end efficiency of 87% is achieved at a maximum available power of 446.6μW from two PV cells, and the quiescent current is only 270nA. An input-offset-storage autozeroing technique is used for opamp offset cancellation in order to achieve the high-accuracy gas detection. A modified split-capacitor digital-to-analog converter (DAC) architecture is used for achieving small area in the signal-processing block.

Keywords: self-powered, gas sensor, photovoltaic energy harvesting, boost converter, offset cancellation.

Abstract: 선 센서 노드에 적합한 자가 전원 가스 센서 집적 회로를 0.18μm CMOS 공정에서 설계하였다. 가스 센싱 필름으로 덮힌 PV 셀을 사용하면서 제안된 센서 시스템은 저전력, 저면적으로 설계가 가능하였다. 시스템이 가스에 노출되었을 때 두 PV 셀로부터 효율적으로 에너지를 획득하기 위해 기존의 PV 셀을 병렬로 연결하는 방법 대신 듀얼-인풋 공유 인덕터 부스트 컨버터를 사용하였다. 이를 통해 200ppm 의 이산화질소 가스 농도에서 전압 변환 효율이 17% 향상되었다. 두 PV 셀로부터 최대 446.6 μW 를 획득하면서 최대 효율 87%를 달성하였고, 이때 대기 전류는 270nA 이다. 정확한 가스 탐지를 위해 연산증폭기 오프셋 제거 방법 중 하나인 입력-오프셋-스토리지 오토제로잉 방법을 사용하였다. 신호 처리 블럭에서 저면적 구현을 위해 스플릿-커패시터 디지털-아날로그 컨버터를 사용하였다.

Keywords: 자가 전원, 가스 센서, 광전지 에너지 하베스팅, 부스트 컨버터, 오프셋 제거.

Table of Contents

Table of Contents……...i
List of Tables……iii
List of Figures……...iv
Chapter 1. Introduction 1
1.1 Motivation 1
1.2 Thesis Outline 1
Chapter 2. Nitrogen Dioxide Gas (NO_2) Sensor and Previous Work 2
2.1 Effects of NO_2 2
2.2 NO_2 Sensor Types 2
2.2.1 Metal oxide based chemiresistive type 3
2.2.2 Electrochemical type 3
2.2.3 Colorimetric type 4
2.3 Previous Work of Colorimetric Sensor 4
Chapter 3. Proposed Gas Sensor System 6
3.1 Self-powered Gas Sensor 6
3.1.1 Working principle 6
3.1.2 Sensor characteristic 7
3.2 Proposed Gas Sensor System 9
3.2.1 Wireless Gas Sensor Node 9
3.2.2 Fundamentals of Photovoltaic Energy Harvesting 9
3.2.3 Maximum power point tracking (MPPT) 10
3.2.4 System Operation 11
Chapter 4. Design of the Self-Powered Gas Sensor IC 13
4.1 Design Goals and Environment 13
4.2 Proposed DC-DC Converter Architecture 13
4.3 Block Diagram of the IC 15
4.4 Design of Important Blocks 16
4.4.1 Power On Reset (POR) and Oscillator (OSC) 16
4.4.2 MPPT 19
4.4.3 Boost an LED Control 21
4.4.4 Gas signal Processing 24
Chapter 5. Implementation Results and Discussions 29
5.1 IC Layout 29
5.2 Energy Harvesting Results (Post-layout) 29
5.3 Gas Signal Processing Results (Post-layout) 33

5.4 Power Breakdown (Post-layout) 35
Chapter 6. Conclusion and Future Work 36
References……...37
Acknowledgments……...38
Curriculum Vitae……39

List of Tables

Table 3.1 Comparison of MPPT methods for energy harvesting and gas sensing purposes 11
Table 5.1 Comparison of Energy Harvesting Converters 33
Table 5.2 Summary of ADC performances 34

List of Figures

Figure 2.1 Effects of NO2 on human health 2
Figure 2.2 Structure of metal oxide based chemisresistive sensor [1] 3
Figure 2.3 Structure of electrochemical sensor [2] 3
Figure 2.4 Structure of colorimetric sensor 4
Figure 2.5 Principle configuration of the portable measuring device [3] 4
Figure 3.1 (a) Principle configuration of Self-powered gas sensor (b) The sensor film before gas exposure (c) The sensor film after gas exposure 6
Figure 3.2 Relationship between NO_2 concentrations and the current change [4] 7
Figure 3.3 I-V characteristic of PV cell before and after gas exposure 7
Figure 3.4 Relationship between NO2 concentrations and the voltage change 8
Figure 3.5 Proposed wireless sensor node 9
Figure 3.6 PV cell I-V characteristics 9
Figure 3.7 Conventional PV EH system 10
Figure 3.8 Gas concentration extraction based on the outputs of MPPT methods 10
Figure 3.9 PV cell I-V characteristics of FOCV MPPT 11
Figure 3.10 Simplified system configuration 11
Figure 3.11 Operation flow of the system 12
Figure 4.1 Boost converter with two PV cells in parallel 13
Figure 4.2 Two parallel PV cells I-V characteristics before gas exposure 14
Figure 4.3 Two parallel PV cells I-V characteristics after gas exposure 14
Figure 4.4 Boost converter with two PV cells are harvested separately 14
Figure 4.5 Dual-Input Shared-Inductor Boost Converter 15
Figure 4.6 Simplified Diagram of the IC 15
Figure 4.7 POR and OSC Diagram 16
Figure 4.8 Comparator of the POR Circuit [7] 16
Figure 4.9 Current-starved ring OSC 17
Figure 4.10 Multiplexer 17
Figure 4.11 Comparator for the select signal 18
Figure 4.12 (a) Capacitor-Less LDO (b) Voltage reference 18
Figure 4.13 MPPT diagram 19
Figure 4.14 MPPT diagram of one PV cell 19
Figure 4.15 MPPT waveforms 20
Figure 4.16 Sample and Hold clock generation diagram [8] 20
Figure 4.17 Sample and Hold clock generation waveforms 21

Figure 4.18 Boost control circuit with MPPT circuit 21
Figure 4.19 On-Time Generation circuit 21
Figure 4.20 Off-Time Generation circuit [9] 22
Figure 4.21 Boost control current waveform 22
Figure 4.22 Dual-Input Shared-Inductor boost converter diagram 23
Figure 4.23 Current waveform of Dual-Input Shared-Inductor boost converter 23
Figure 4.24 Dual-Input Shared-Inductor Boost Control Cituit 23
Figure 4.25 LED control diagram 23
Figure 4.26 Gas signal processing diagram 24
Figure 4.27 Timing operation of the offset cancellation 24
Figure 4.28 Opamp Subtractor with Autozero Offset Cancellation circuit 25
Figure 4.29 Two-stages Opamp circuit 25
Figure 4.30 10-bit SAR ADC diagram 25
Figure 4.31 Conventional Split-capacitor DAC architecture 26
Figure 4.32 Modified bridge solution DAC architecture 26
Figure 4.33 Proposed 10-bit Split-cap SAR ADC 26
Figure 4.34 Self-calibrating comparator 27
Figure 4.35 Timing operation of the self-calibrating comparator 28
Figure 5.1 IC Layout and Area Breakdown 29
Figure 5.2 Boost and LED Control waveforms 29
Figure 5.3 MPPT Waveforms 30
Figure 5.4 (a) Dual-Input Shared-Inductor waveforms (b) Enlarged view at 376ms 31
Figure 5.5 Dual-Input Shared-Inductor Boost Converter End-to-End Efficiency 32
Figure 5.6 End-to-End Efficiency with the different gas concentrations 32
Figure 5.7 10-bit SAR ADC Static Performances 33
Figure 5.8 10-bit SAR ADC Dynamic Performances 34
Figure 5.9 Power Breakdown 35

Chapter 1. Introduction

1.1 Motivation

Gas leaks is one of the biggest challenges many workplaces is facing because it leads to severe health problems. Therefore, it is very important to detect the existence of toxic gases for the health care application.

Wireless Sensor Nodes (WSN) can be used to measure the gas condition of many points in the workplace. Usually, a WSN consists of a sensing unit, a wireless transceiver, and a battery. Because the battery life is the main issue in the WSN, the energy harvesting systems are developed to increase the autonomy of the nodes. However, an energy harvesting unit (EHU) is required to harvest energy from energy sources. As a result, it is very difficult to make a compact node.

Thus, it is desireable to reduce the size of the sensor node and make it operate as long as possible. The proposed research work introduces an IC that combines the sensing unit and the EHU. Consequently, the size of the sensor node is greatly reduced, and the power consumption is ultra-low.

1.2 Thesis Outline

A brief organization of this thesis is stated below.

Chapter 2 introduces the effects of nitrogen dioxide gas (NO_2) on human health, the NO_2 sensor types, and a previous work of the colorimetric NO_2 sensor.

Chapter 3 introduces the proposed self-powered gas sensor system with the fundamentals of photovoltaic energy harvesting.

Chapter 4 describes the design of the IC in detail.

Chapter 5 presents the implementation results and discussions.

Chapter 6 shows the conclusions and recommends future research directions.

Chapter 2. Nitrogen Dioxide Gas (NO_2) Sensor and Previous Work

2.1 Effects of NO_2

Internal combustion engines burning fossil fuels are the most prominent sources of NO_2. Outdoors, NO_2 can be a result of traffic from motor vehicles. Indoors, exposure arises from cigarette smoke, butane, kerosene heaters, and stoves.

In many workplaces, NO_2 is used as an intermediate in the manufacturing of chemicals, such as nitric acid, acrylates, and chemical explosives. NO_2 is also created by the engines in industries. Workers are at risk of NO_2 exposure, and they might suffer from many serious health effects.

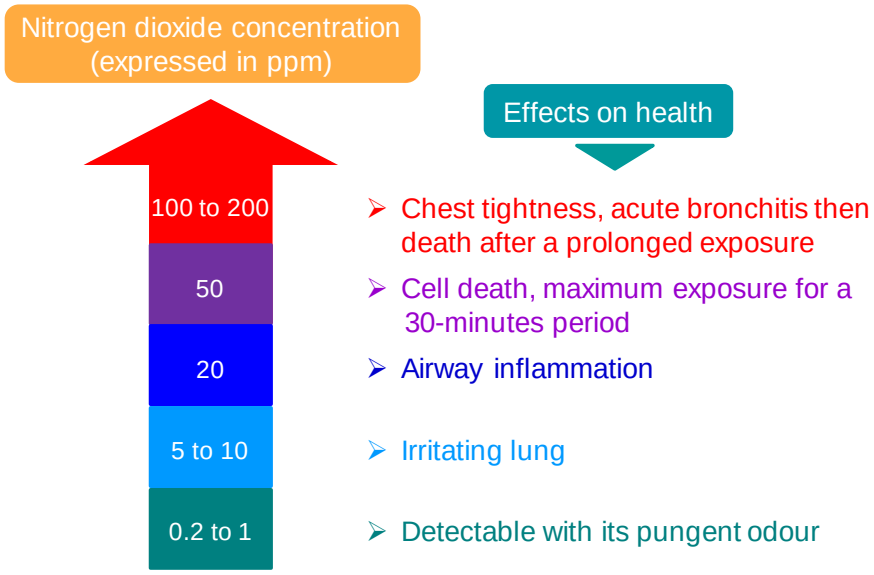

Figure 2.1 Effects of NO2 on human health

As shown in Figure 2.1, if people are exposed to the NO_2 concentration range from 0.2ppm to 200ppm, their health will be significantly affected. For example, the gas concentration range from 5ppm to 10ppm can irritate the lung, and the gas concentration of 20ppm can cause inflammation on the airway. Furthermore, humans might be dead if they are exposed to the high-level gas concentration of 200ppm in a long time.

2.2 NO_2 Sensor Types

There are many kinds of instruments that can be used to measure the gas concentration. Metal oxide based chemiresistive type, electrochemical type, and colorimetric type are the three most widely used sensors. These sensor types will be introduced below.

2.2.1 Metal oxide based chemiresistive type

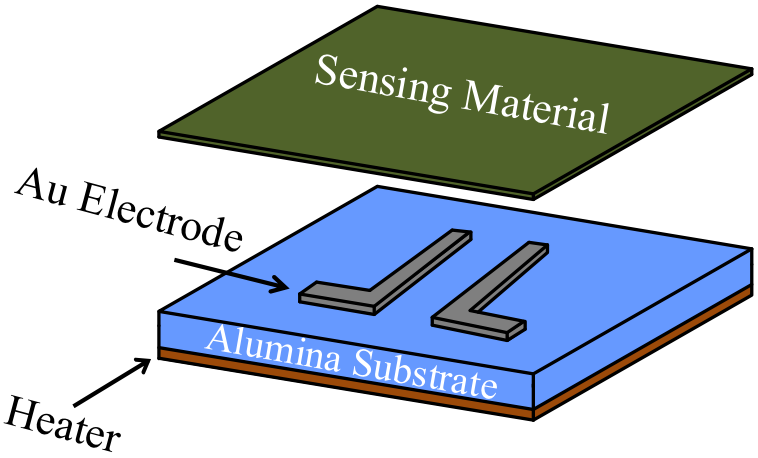

Figure 2.2 Structure of metal oxide based chemisresistive sensor [1]

As shown in Figure 2.2, the sensor consists of a sensing material, an Au electrode, an alumina substrate, and a back side heater. Pt paste is screen-printed on the back side of the Al_2O_3 substrate to control the operating temperature through the applied voltage. Pt wires are attached to both the Au electrode and the Pt heater with Au paste. Metal oxide paste was screen-printed onto Au electrodes deposited on the Al_2O_3 substrate.

When the sensor is exposed to gases, the sensing material will react with the gas. As a result, the resistance measured on the electrodes will be changed. Based on the resistance change, the gas concentrations are detected.

2.2.2 Electrochemical type

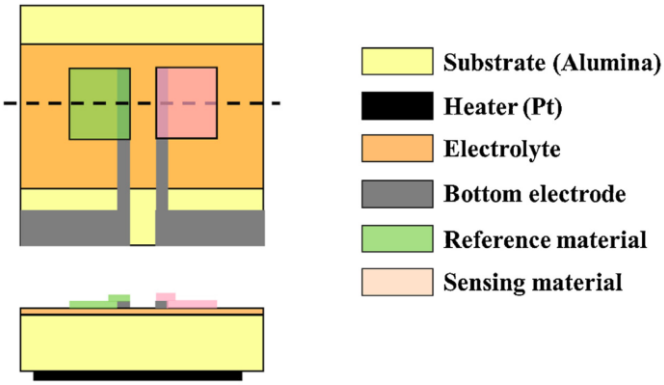

Figure 2.3 Structure of electrochemical sensor [2]

The electrochemical sensor (Figure 2.3) is comprised of a sensing material and a reference material at the top, an electrode, an electrolyte, an Alumina substrate, a heater at the bottom.

The sensing material will react with the gas after gas exposure. Therefore, the electromotive force (EMF) between the reference and sensing electrodes will be changed. Based on the EMF change, the gas concentrations are detected.

2.2.3 Colorimetric type

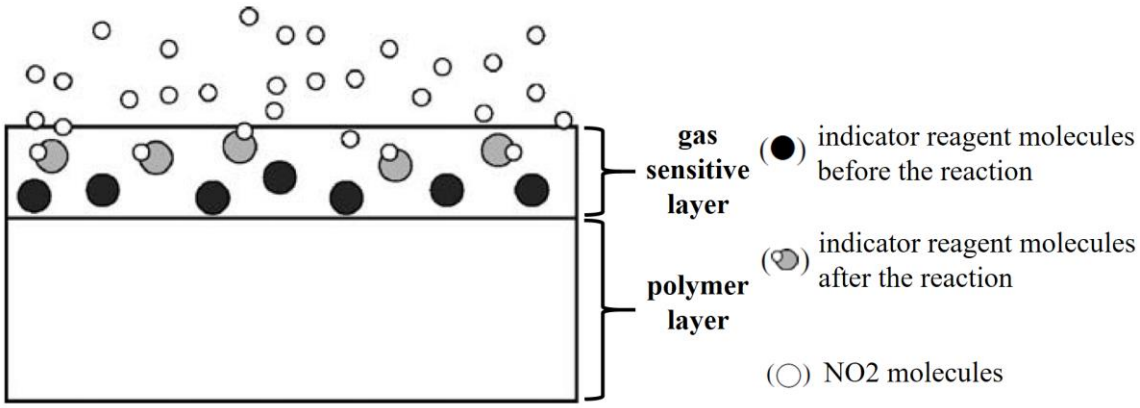

Figure 2.4 Structure of colorimetric sensor

As shown in Figure 2.4, the sensor is a film which is composed of a gas sensitive layer and a polymer layer.

When the sensor is exposed to gases, the sensing material will react with the gas. After the reaction, the color of the gas sensitive layer will be changed. When the light comes to the sensor, the light transmission will be changed because of the color change. By measuring the transmission change, the gas concentrations are detected.

The colorimetric sensor will be discussed in this work.

2.3 Previous Work of Colorimetric Sensor

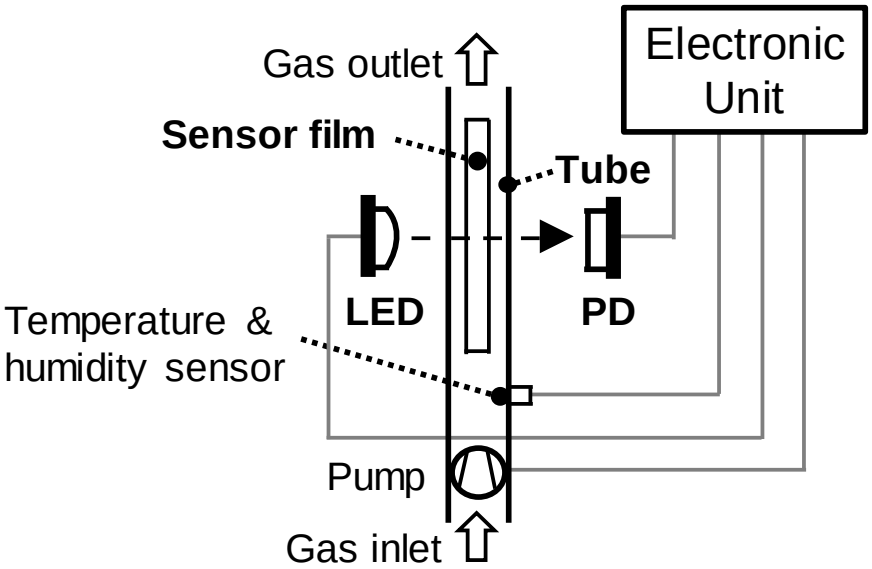

Figure 2.5 Principle configuration of the portable measuring device [3]

The developed sensor chip can be used in portable, battery-powered measuring instruments for detecting outdoor and working place air pollution. The source of light in the device is a LED. The transmission change is detected by a photodiode (PD). The measuring device has to include a sensor for temperature and humidity and a pumping system with constant flow to draw the ambient air through the flow cell with the fixed sensor chip. An evaluation unit is used to save all of the established sensor characteristics (calibration function, temperature influence, etc.).

There are two disadvantages of this device. Firstly, the sensor still consumes electrical power for detection. Secondly, it is difficult to make the device compact because of LED, the senor film, the tube, and PD. Therefore, it is essential to make the low-power sensor with more compact size.

Chapter 3. Proposed Gas Sensor System

3.1 Self-powered Gas Sensor

3.1.1 Working principle

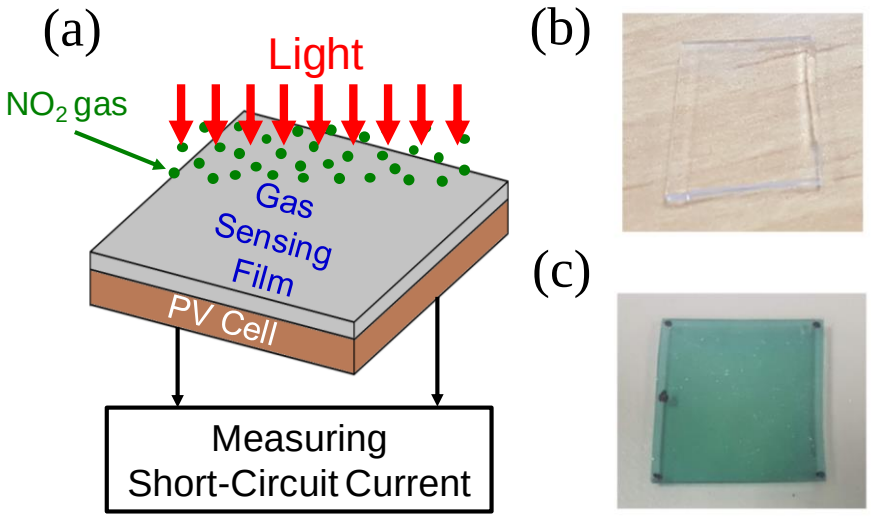

Figure 3.1 (a) Principle configuration of Self-powered gas sensor (b) The sensor film before gas exposure (c) The sensor film after gas exposure

A colorimetric gas sensor that is developed overcomes all the disadvantages of the previous work. The sensor can power itself, and its size is small as it does require other components, such as LED, tube, and PD.

The principle configuration of the sensor is shown in Figure 3.1 (a). A PV cell is covered by the sensor film [4]. Before gas exposure, the sensor film is transparent (Figure 3.1 (b)). After gas exposure, the sensor film color is changed (Figure 3.1 (c)). As a result, the light transmission is changed when the light comes to the film. The light transmission change during NO_2 exposure is detected by measuring the short-circuit current (I_{SC}) output of the PV cell because the transmission change is in proportion to the current change. However, the source meter is used for measuring the current, so an IC with energy harvesting and gas sensing functions is needed in order to make a gas sensor system.

3.1.2 Sensor characteristic

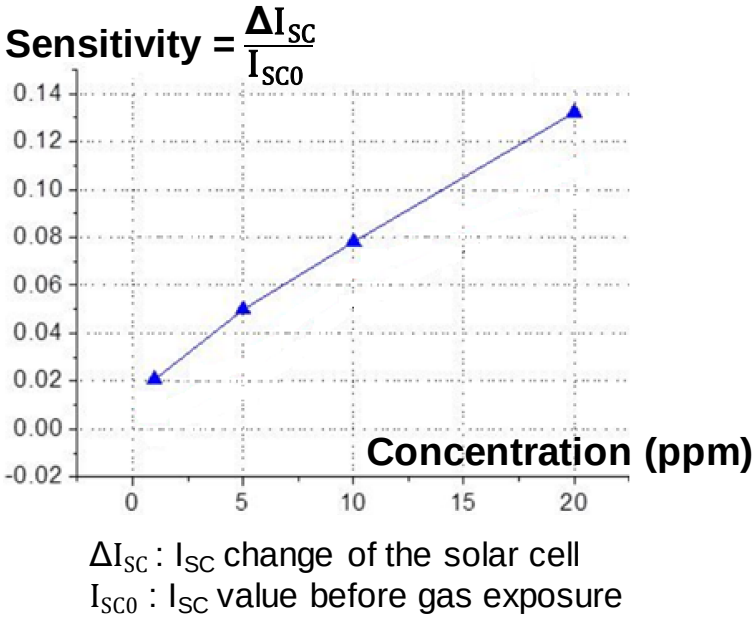

Figure 3.2 Relationship between NO_2 concentrations and the current change [4]

As shown in Figure 3.2, there is a relationship between the gas concentration (in ppm) and the sensitivity which is equal to the current change over the current value before gas exposure. The relationship is almost linear. Therefore, with a constant gas concentration, we have a constant fraction of the current change and the current value before gas exposure. In other words, the gas concentration is a function of this fraction ($C_{NO2} = f(\frac{\Delta I_{SC}}{I_{SC0}})$) or the current change is a function of the gas concetration ($\frac{\Delta I_{SC}}{I_{SC0}} = f(C_{NO2})$).

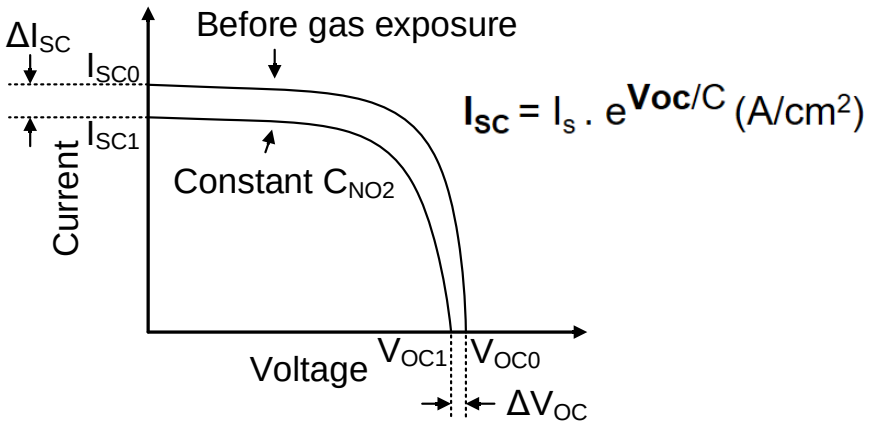

Figure 3.3 I-V characteristic of PV cell before and after gas exposure

In fact, we also found that the gas concentration has a relationship with open-circuit voltage (V_{OC}) of the PV cell based on the PV cell I-V characteristic (Figure 3.3).

$$I_{SC} = I_s . e^{Voc/C} (A/cm^2), \text{ where } I_s, C \text{ are constant} \quad (3.1)$$

$$\frac{\Delta I_{SC}}{I_{SC0}} = f(C_{NO2}) = \frac{I_{SC0} - I_{SC1}}{I_{SC0}} = 1 - \frac{I_{SC1}}{I_{SC0}} \rightarrow \frac{I_{SC1}}{I_{SC0}} = 1 - f(C_{NO2}) \quad (3.2)$$

$$\frac{I_{SC1}}{I_{SC0}} = \frac{I_s \cdot e^{Voc1/C}}{I_s \cdot e^{Voc0/C}} = e^{(Voc1-Voc0)/C} = 1 - f(C_{NO2}) \quad (3.3)$$

The short-circuit current is an exponential function of V_{OC}, where I_s and C are constant (3.1). There are the curves of the characteristic before gas exposure and after a constant gas concentration exposure. As a result, the gas exposure creates the current change (ΔI_{SC}) as well as the voltage change (ΔV_{OC}). As mentioned, the fraction of the current change over the current value before gas exposure is a function of the gas concentration, so the fraction of the current value after gas exposure over the current value before gas exposure is also a function of the gas concentration (3.2). Replace I_{SC} from equation (3.1) to (3.2), we get (3.3). I_s is canceled out, so we have $e^{(Voc1-Voc0)/C}$ is a function of the gas concentration. Because C is constant, we get $\Delta V_{OC} = V_{OC1}-V_{OC0} = \ln[1 - f(C_{NO2})]/C$. That means the gas concentration is a function of voltage change ($C_{NO2} = f(\Delta V_{OC})$).

Figure 3.4 shows the relationship between gas concentrations and the voltage change, which is calculated from experiment result with the sensor films and the approximation.

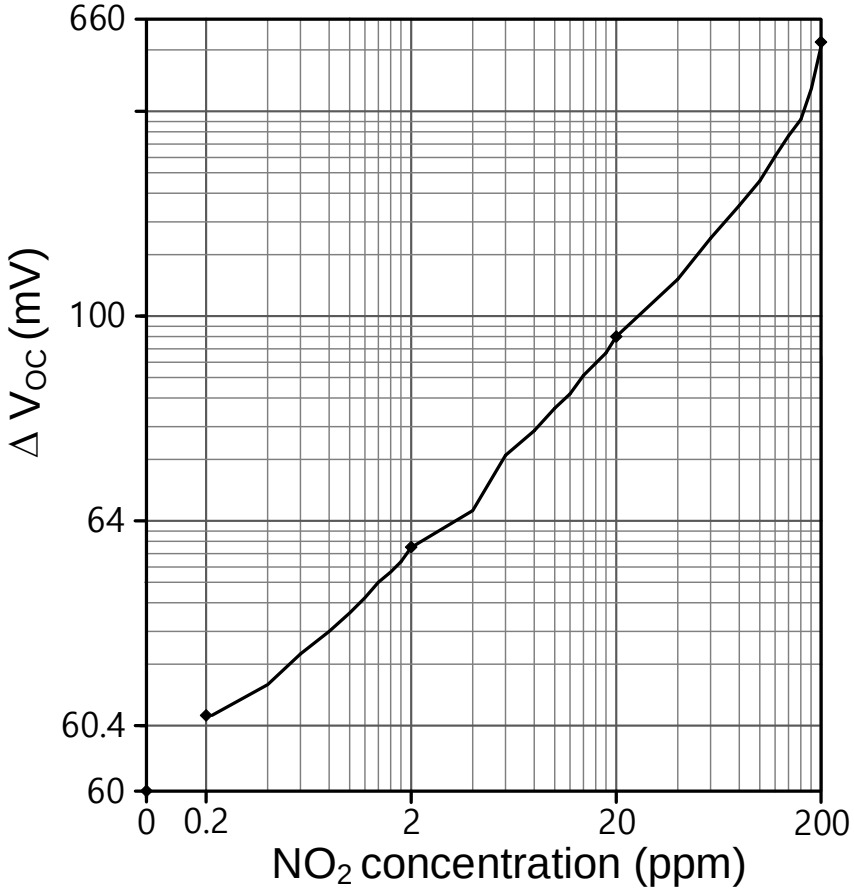

Figure 3.4 Relationship between NO2 concentrations and the voltage change

3.2 Proposed Gas Sensor System

3.2.1 Wireless Gas Sensor Node

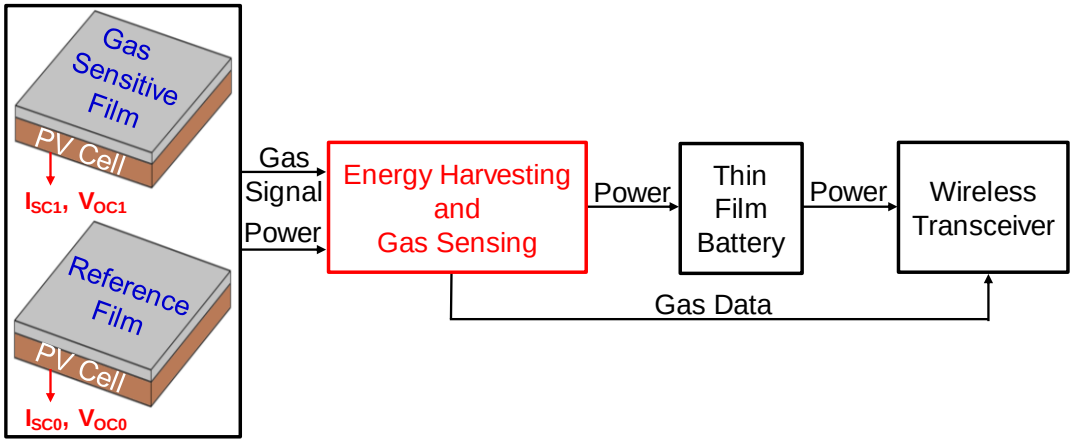

Figure 3.5 Proposed wireless sensor node

A proposed wireless sensor node is shown Figure 3.5. This work aims at wireless sensor networks for the indoor NO_2 analysis application, and the proposed system plays the role of a wireless sensor node. Two PV cells are covered by two sensor films. One film is the gas sensitive film, another one is the reference film. To detect the gas concentration, the IC (in red) measures the output current change or the output voltage change on the PV cells based on the color change of the gas sensitive film when the film is exposed to NO_2. At the same time, the IC harvests power from the PV cells to charge the battery. A wireless transceiver is powered by a battery and receives gas data from the IC. The targets are 0.4V-1.1V input and 3V output, so a boost converter is used for PV energy harvesting.

3.2.2 Fundamentals of Photovoltaic Energy Harvesting

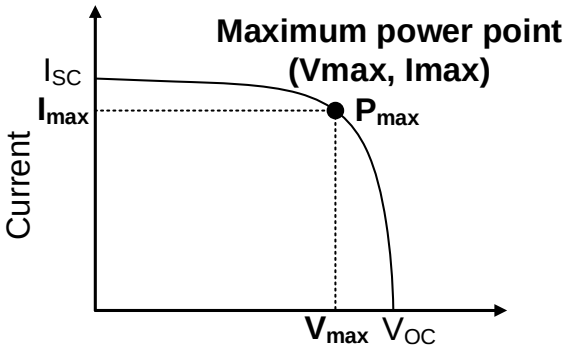

Figure 3.6 PV cell I-V characteristics

In the PV cell I-V characteristics (Figure 3.6), there is a point at which the PV cell gets the maximum power.

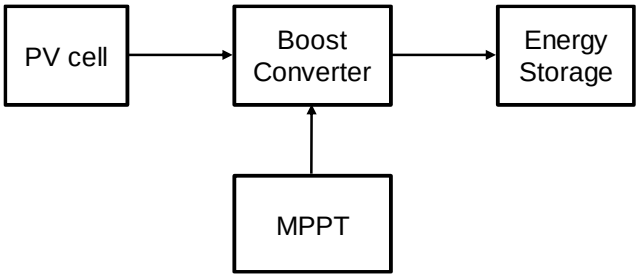

Figure 3.7 Conventional PV EH system

As shown in Figure 3.7, there is a conventional PV EH system. Power is delivered from the PV cell to energy storages, such as a battery or a supercapacitor. The boost converter is used to control the operating point of the PV cell, and a MPPT method is used for regulating the PV cell to the maximum power point, so the system can achieve a maximum energy delivery from the PV cell to the energy storage.

3.2.3 Maximum power point tracking (MPPT)

There are three most popular MPPT methods, including Fractional Short-Circuit Current (FSSC), Fractional Open-Circuit Voltage (FOCV), and Perturb and Observe (P&O). These methods can be used for the proposed gas sensor system.

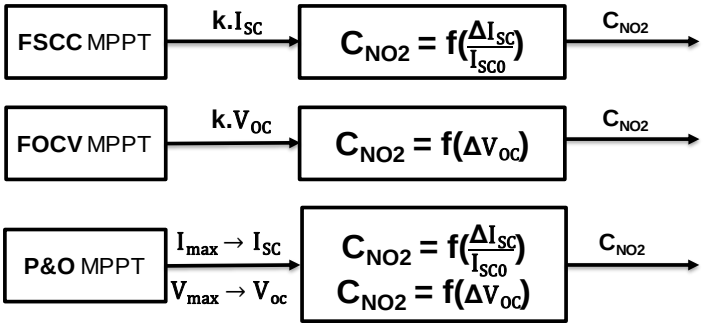

Figure 3.8 Gas concentration extraction based on the outputs of MPPT methods

As shown in Figure 3.8, from FSSC MPPT, we can get $k.I_{SC}$, $k.\Delta I_{SC}$ and use the relationship between the gas concentrations and the current change to extract the gas concentrations. Similarly, from FOCV MPPT, we can get $k.V_{OC}$, $k.\Delta V_{OC}$ and use the relationship between the gas concentrations and the voltage change to extract the gas concentrations. From P&O, we can get both ΔI_{SC} and ΔV_{OC}. Then using the relationship between the gas concentrations and the current change or the relationship between the gas concentrations and the voltage change to extract the gas concentrations.

As given in Table 3.1, FSCC uses a current sensor and an additional switch to short the PV cell in order to measure I_{SC}, so it requires high implementation complexity. FOCV does not require a complicated control system, so it is easy to implement. P&O has simple structure and operation, so it is easy to implement. P&O does not directly sample V_{OC} and I_{SC}, so it requires a circuit to convert V_{max} to V_{OC} and I_{max} to I_{SC}. As a result, it creates errors and low detection accuracy. FSCC and FOCV directly sample I_{SC} and V_{OC}, so it is high detection accuracy.

FOCV MPPT is the best method for both energy harvesting and gas sensing functions because it requires a low implementation complexity and achieves a high gas sensing accuracy. Therefore, FOCV MPPT is used for the IC.

Table 3.1 Comparison of MPPT methods for energy harvesting and gas sensing purposes

MPPT	Implementation complexity	Efficiency	Convergence speed	Sensed parameters	C_{NO2} Accuracy
FSCC	Medium	High	Medium	Current	High
FOCV	Low	High	Medium	Voltage	High
P&O	Low	High	Varies	Voltage Current	Low

The FOCV MPPT method (Figure 3.9) is used to regulate the PV to the maximum power point. At this point, the maximum voltage (V_{max}) is equal to a fraction of the open circuit voltage with k in the range from 0.71 to 0.78 [5]. The FOCV method samples $k.V_{OC}$ and then regulates the PV cell voltage to $k.V_{OC}$, which means the PV cell is operating at the maximum power point.

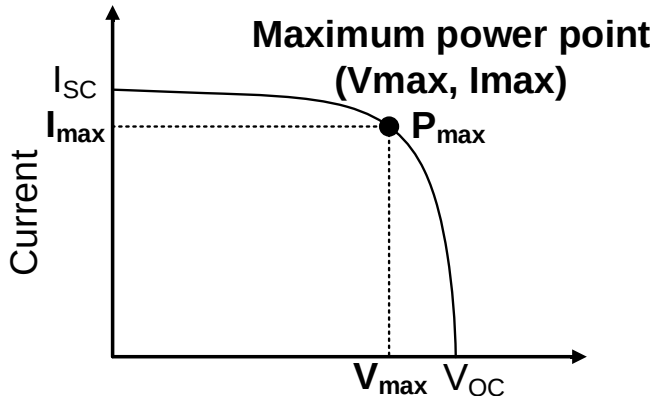

Figure 3.9 PV cell I-V characteristics of FOCV MPPT

3.2.4 System Operation

Figure 3.10 shows the system configuration of the system, and Figure 3.11 shows the operation flow of the system. When the ambient light is sufficient, energy will be transfer from the PV cell to the battery. In addition, the LED is off, and V_{OC} from MPPT block will be used for gas sensing. If there is not enough ambient light, the LED will be turned on to supply the light for the PV cell, so we still have V_{OC} for gas sensing.

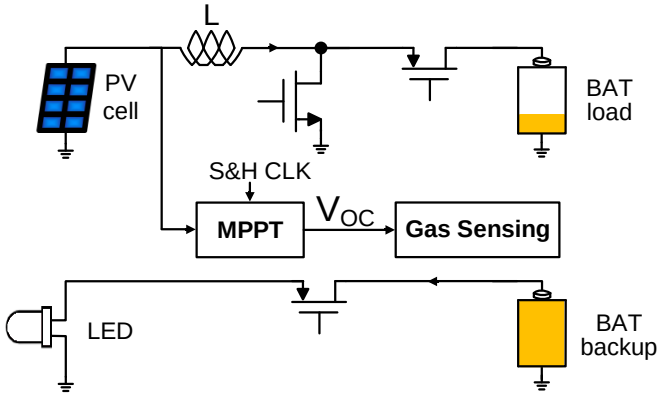

Figure 3.10 Simplified system configuration

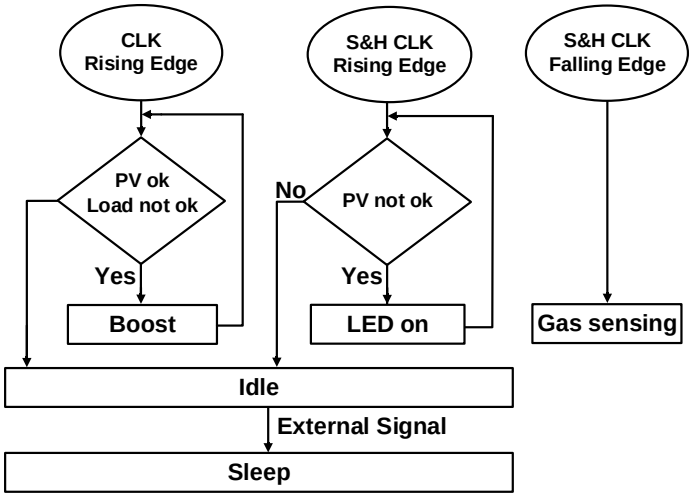

Figure 3.11 Operation flow of the system

Chapter 4. Design of the Self-Powered Gas Sensor IC

4.1 Design Goals and Environment

Design goals:

- Input voltage: 400mV to 1.1V
- Output voltage: Thin film battery 3V
- MPPT: samples an accurate V_{OC}
- Boost converter:
  - High efficiency (~85%)
  - Low quiescent current (~300nA)
- Gas signal processing:
  - Low offset (100 μV),
  - Low power (~1μW)
  - High ADC performances
  - Covers the health care detection range (0.2ppm-200ppm)

Design environment:

- Simulation Environment: Cadence – Virtuoso Analog Design
- Process: 0.18μm CMOS 1-Poly 6-Metal

4.2 Proposed DC-DC Converter Architecture

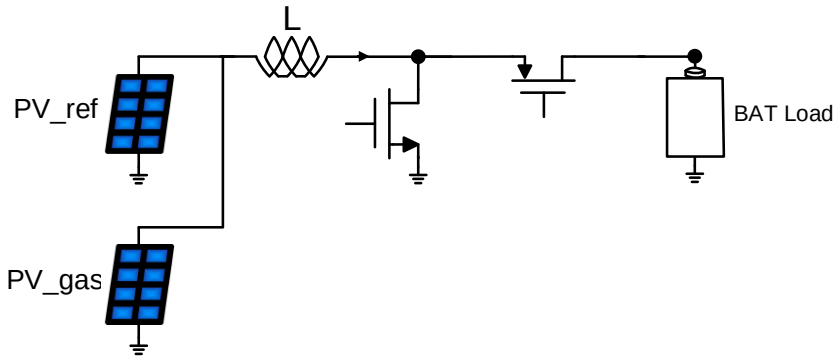

Figure 4.1 Boost converter with two PV cells in parallel

There are two PV cells, and we want to harvest energy from these PV cells, so we can connect them in parallel (Figure 4.1). However, we have two cases, the first case is before gas exposure and another one is after gas exposure. In the case before gas exposure, it is efficient to connect two PV cells in parallel since the maximum power of two parallel PV cells is equal to the sum of the maximum powers of two PV cells based on the characteristic in Figure 4.2. In contrast, in the case after gas exposure, the end-to-end efficiency will be decreased because of the decrease of maximum power on two parallel cells, which is the input power of the boost converter based on the characteristic in Figure 4.3. The higher gas concentrations are exposed, the lower end-to-end efficiency is.

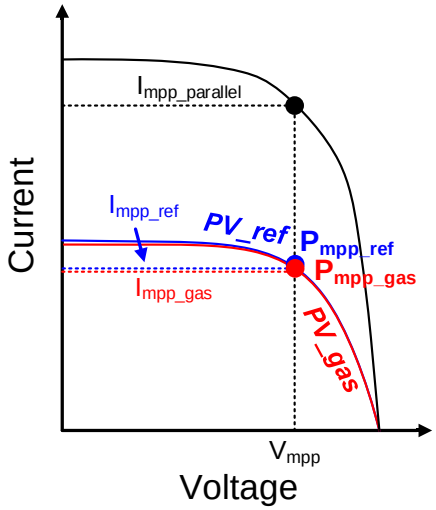

Figure 4.2 Two parallel PV cells I-V characteristics before gas exposure

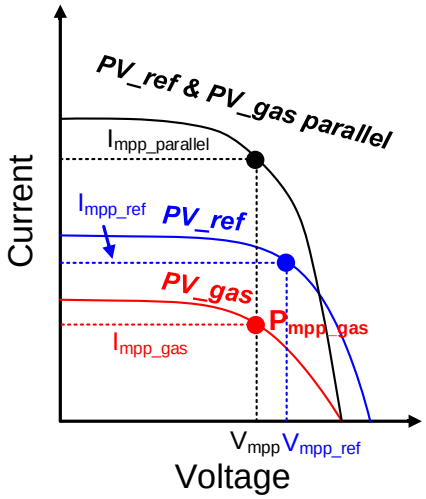

Figure 4.3 Two parallel PV cells I-V characteristics after gas exposure

To solve this issue, we can harvest energy from two cells separately (Figure 4.4). However, this topology requires two inductors. Therefore, we proposed dual-input shared-inductor topology (Figure 4.5) [6] to solve this problem. By using this topology, we can harvest energy from two PV cells efficiently with only one inductor, which saves the cost and area.

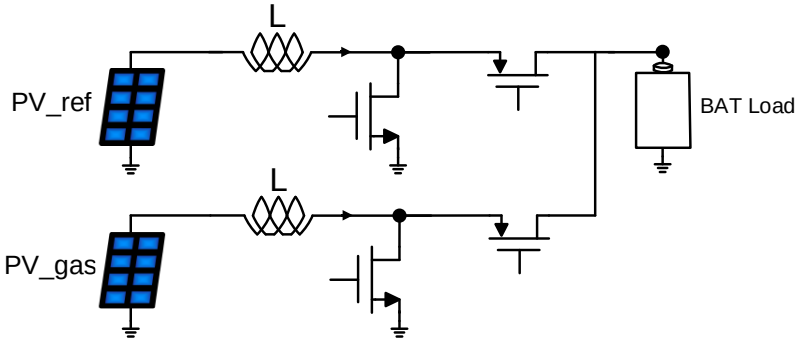

Figure 4.4 Boost converter with two PV cells are harvested separately

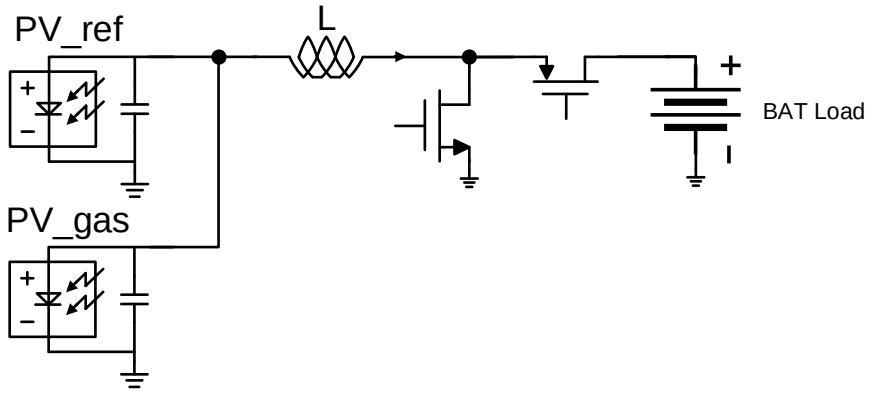

Figure 4.5 Dual-Input Shared-Inductor Boost Converter

4.3 Block Diagram of the IC

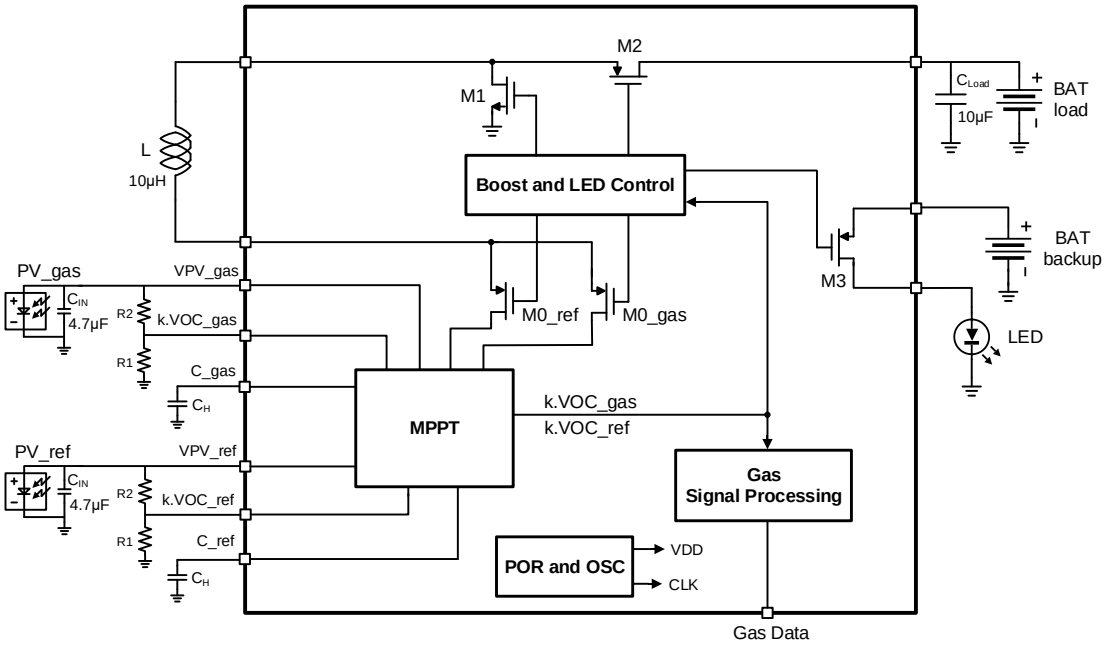

Figure 4.6 Simplified Diagram of the IC

Figure 4.6 shows simplified diagram of the IC. It has four main blocks, including a power on reset (POR) and oscillator (OSC) block, a MPPT block, a boost and LED control block, and a gas signal processing block. It also has four power switches of the boost converter and one power switch of LED control.

The POR and OSC block has a POR circuit which is used to start up the IC when there is enough light ambient and provides the power supply voltage (VDD) for the IC. The oscillator is used to provide the clock signal for the IC.

The MPPT block is used to sample the maximum power point voltages on both the PV cell with the gas sensitive film (PV_gas) and on the PV cell with the reference film (PV_ref).

The boost control is used to regulate the PV cell to the maximum power point and the LED control is used to turn on or turn off LED. If there is not enough ambient light, the LED will be turned on to supply the light for PV cells, so we still have open circuit voltage for gas sensing.

The gas signal processing block is used to extract the gas concentration data.

4.4 Design of Important Blocks

4.4.1 Power On Reset (POR) and Oscillator (OSC)

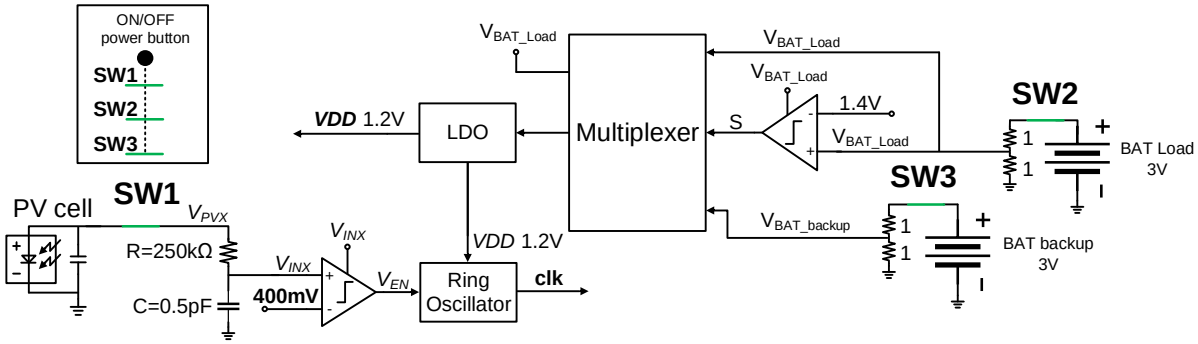

Figure 4.7 POR and OSC Diagram

There are three physical switches (SW1, SW2, SW3) are used to connect the IC with the PV cell, the load battery, and the backup battery (Figure 4.7). The POR circuit consists of a RC delay circuit and a comparator. The POR circuit pulls the enable signal (V_{EN}) high when the voltage on PV cell ≥ 400mV which means the ambient light is sufficient. If the enable signal exists before the VDD, the ring OSC might not function accurately. Therefore, the RC circuit is used to create a delay for the enable signal.

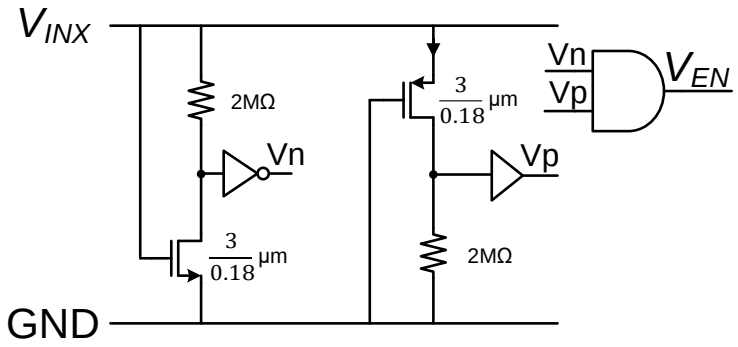

Figure 4.8 Comparator of the POR Circuit [7]

As shown in Figure 4.8, the comparator of the POR circuit are comprised of two branches. One branch has a NMOS and a resistor, another one has a PMOS and a resistor. The outputs of these branches are the inputs of a NAND gate. When V_{IN} reaches the threshold of the circuit, Vn and Vp go high makes the enable signal goes high. This circuit has simple implementation and low power consumption.

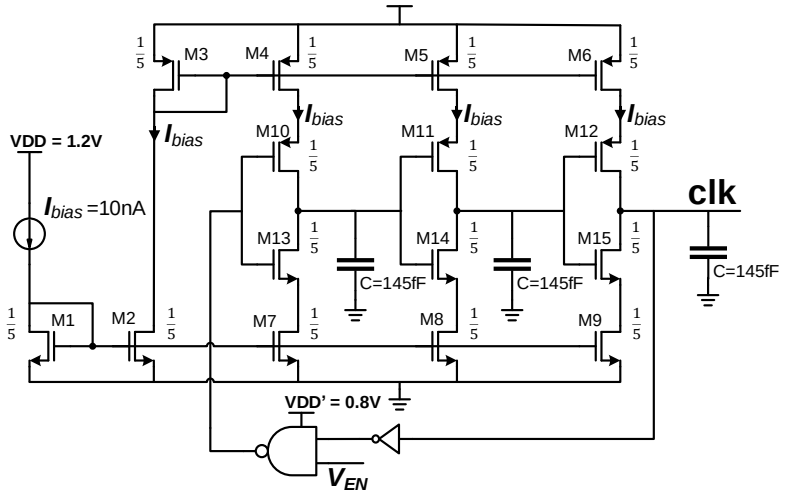

Figure 4.9 Current-starved ring OSC

Figure 4.9 shows the oscillator circuit which provides a 10kHz clock frequency. A three stages current-starved ring oscillator is used because of its low power consumption. The OSC receives the enable signal from POR circuit through a NAND gate. When the enable signal goes high, the oscillator will start generating the clock.

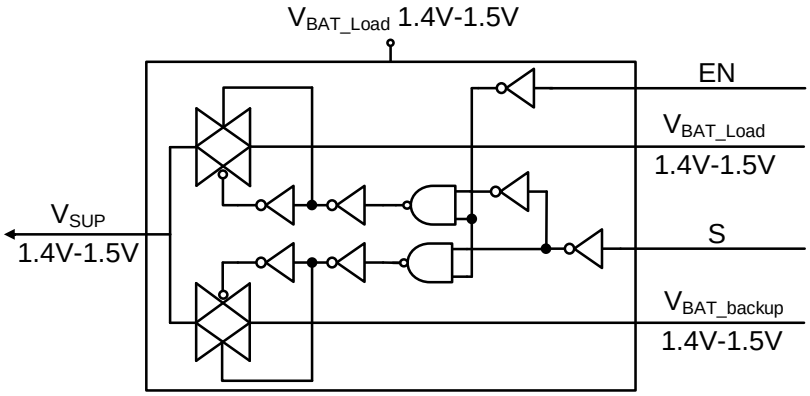

Figure 4.10 Multiplexer

The VDD is supplied by the load battery (BAT Load) or the backup battery (BAT backup). A multiplexer (Figure 4.10) is used to select which one will supply the voltage for the VDD. The comparator that creates the select signal "S" (Figure 4.11) uses the same structure with the comparator of the POR circuit. In the beginning, if the load battery is not ready, the VDD is supplied by the backup battery. When the load battery is ready which means the node voltage V_{BAT_BACKUP} 1.2V from the load battery reaches 1.2V, the select voltage will go high. As a result, the VDD is supplied by the load battery.

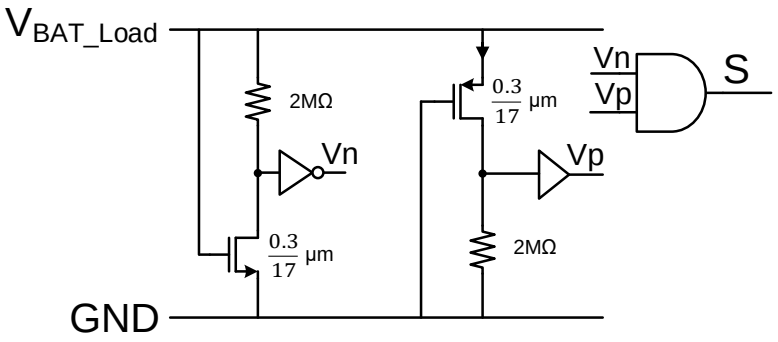

Figure 4.11 Comparator for the select signal

The LDO circuit is shown in Figure 4.12. The circuit has phase margin of 85^0 at V_{SUP} = 1.4V-1.5V and I_{OUT} = 10nA-10µA, so the circuit is stable in the required operation conditions.

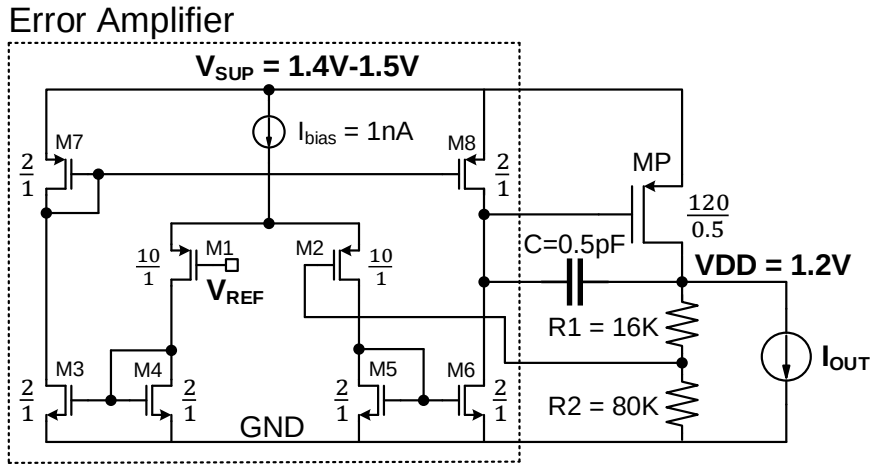

(a)

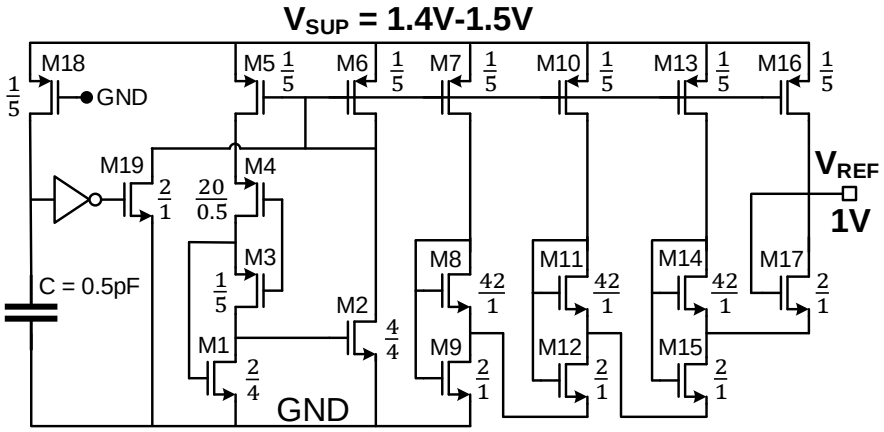

(b)

Figure 4.12 (a) Capacitor-Less LDO (b) Voltage reference

4.4.2 MPPT

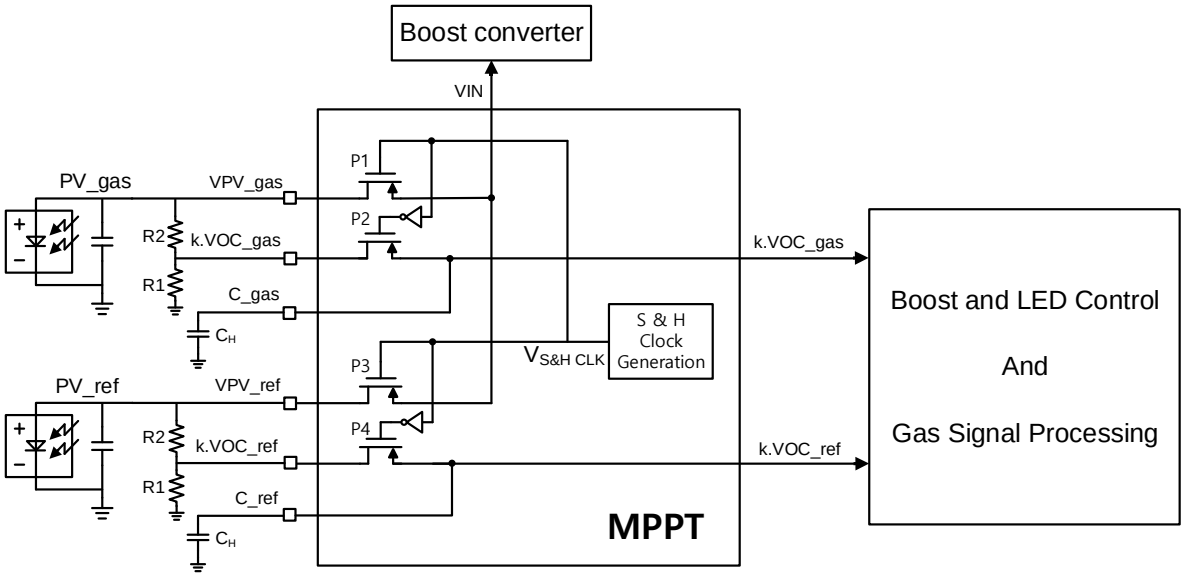

Figure 4.13 MPPT diagram

As shown in Figure 4.13, it is an open circuit voltage based MPPT. Therefore, the IC samples and holds a fraction of V_{OC} on the external capacitor (C_H). Then boost controller will regulate input voltage of the PV cell to the held value on the capacitor. This block consists of a sample and hold clock generator and four switches.

The operation of MPPT circuit for one PV cell is shown in Figure 4.14 and Figure 4.15. Firstly, the sample and hold clock generator creates the clock for the switches. During the sample period, P1 is off and P2 is on. A fraction of the open circuit voltage will be held on the capacitor. During the hold time, P1 is on and P2 is off, the V_{MPP} will be held on the capacitor until the next cycle of the clock.

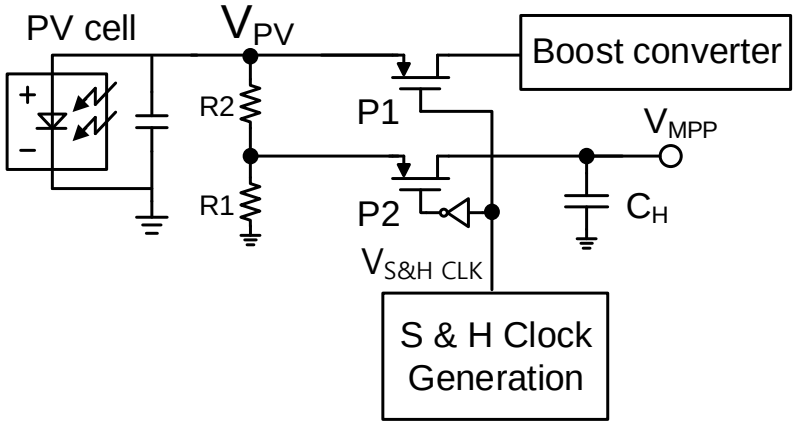

Figure 4.14 MPPT diagram of one PV cell

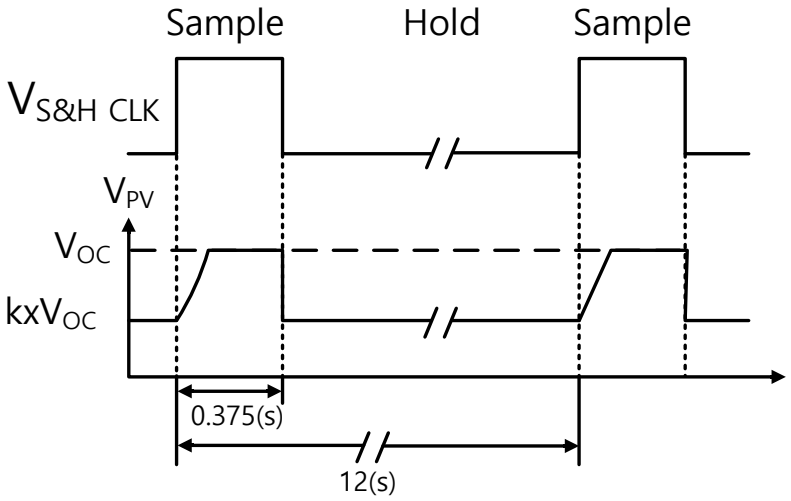

Figure 4.15 MPPT waveforms

The sample and hold clock generation circuit operation is shown in Figure 4.16 and Figure 4.17. A pulse width modulation is used to generate the required sample and hold clock. The frequency is 1/12 Hz, which is suitable for both energy harvesting and gas sensing functions. The branch on the left is used to generate the current I_1. Then the current is copied to another branch for charging the capacitor C_T. The capacitor is discharged by the current I_2 through an NMOS. Therefore, we have a ramp signal at the node V_{RAMP}. The ramp signal is fed into a comparator which has a reference voltage V_A. Through a RS Flip Flop, we can get the desired sample and hold clock (Figure 4.17). The sample and hold time are controlled by the reference voltage V_A of the comparator.

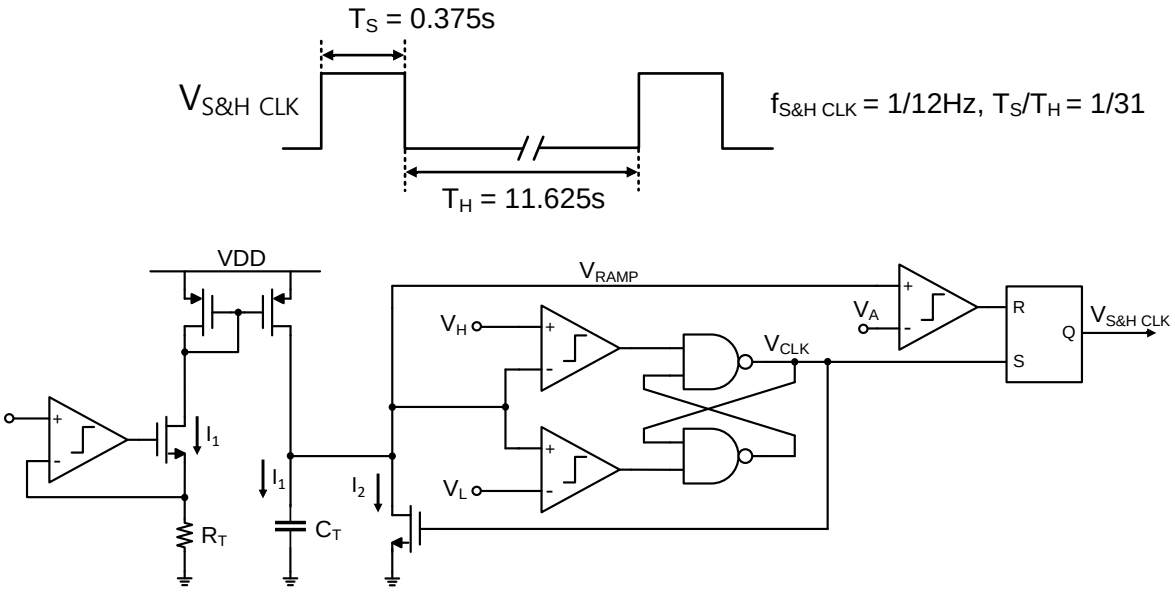

Figure 4.16 Sample and Hold clock generation diagram [8]

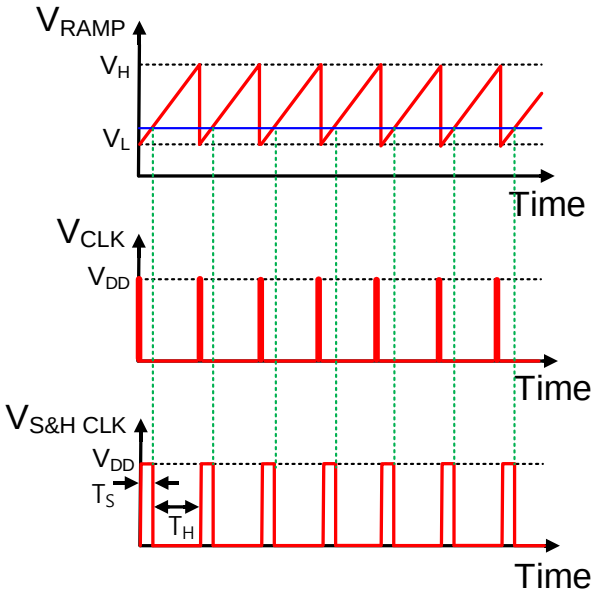

Figure 4.17 Sample and Hold clock generation waveforms

4.4.3 Boost an LED Control

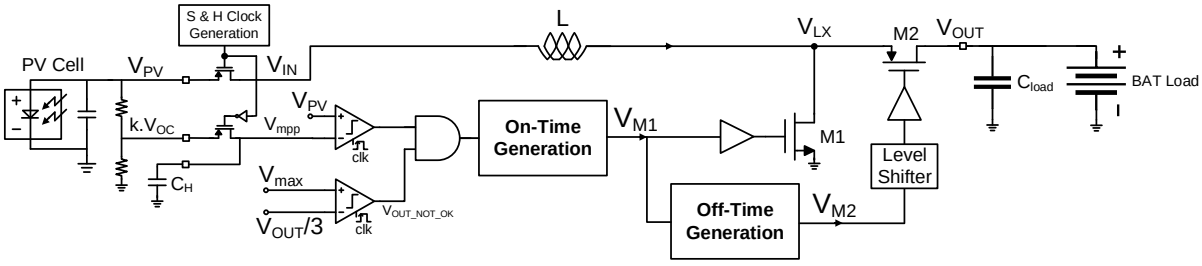

Figure 4.18 Boost control circuit with MPPT circuit

Figure 4.18 shows the boost converter with the boost control circuit with MPPT circuit. For simplicity, only one PV cell is shown. V_{IN} is the input of the boost converter, which consists of an inductor, a low-side power switch, and a high-side power switch. Two dynamic comparators are used to compare V_{PV} and V_{mpp} for MPPT purpose and compare $V_{OUT}/3$ and V_{max} for detecting the full-charged load battery. The dynamic comparators are used because of their low power consumption. The on-time generation is used for building up inductor current. The off-time generation is used for transferring inductor current to BAT Load.

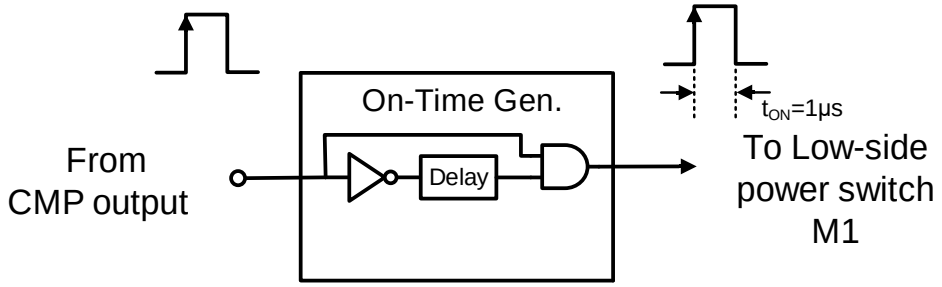

Figure 4.19 On-Time Generation circuit

The on-time generation circuit is shown in Figure 4.19. It is a commonly used circuit, which is composed of a not gate, a delay, and a NAND gate. When the output of the dynamic comparator goes high, the on-time generation will create a pulse of 1μs to drive the low-side power switch.

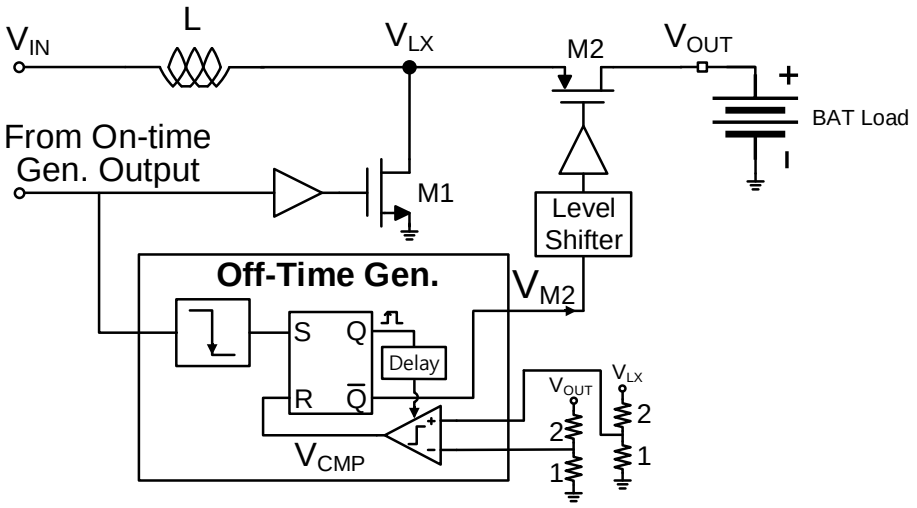

Figure 4.20 Off-Time Generation circuit [9]

The off-time generation circuit is depicted in Figure 4.20. The circuit detects zero-current on the inductor by comparing the switching node V_{LX} and the output node V_{OUT}. Then an SR-FF is used to generate the off-time.

The operation of the boost converter (Figure 4.18) is shown in Figure 4.21. When V_{PV} is larger than V_{mpp}, and $V_{OUT_NOT_OK}$ is high which means the load battery is not full-charged, the power switch M1 is on for 1μs. Once M1 is off, M2 is on for a period t_{OFF} until the inductor current becomes zero. In the case, the load battery is full-charged, there will be no switching.

The advantages of this operation are low power consumption and stable. The power consumption is low because the comparators are only on at the clk rising edge and there is no need for other circuits, such as oscillator, ramp generator, etc. Secondly, it is stable because it is a hysteresis control method, so the IC is cycle by cycle stable, and it is easy to turn on turn off the power switches for MPPT.

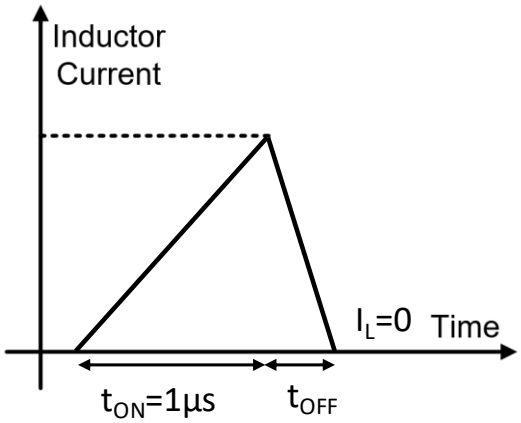

Figure 4.21 Boost control current waveform

The operation of the dual-input shared-inductor boost converter (Figure 4.22) is illustrated in Figure 4.23. At the clk rising edge, M0_ref switch is on, and the PV_ref is harvested. At the clk falling edge, M0_gas switch is on, and the PV_gas is harvested. The dual-input shared-inductor boost control circuit is shown in Figure 4.24.

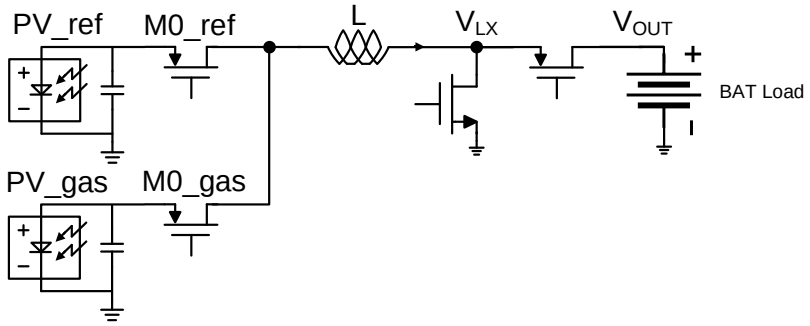

Figure 4.22 Dual-Input Shared-Inductor boost converter diagram

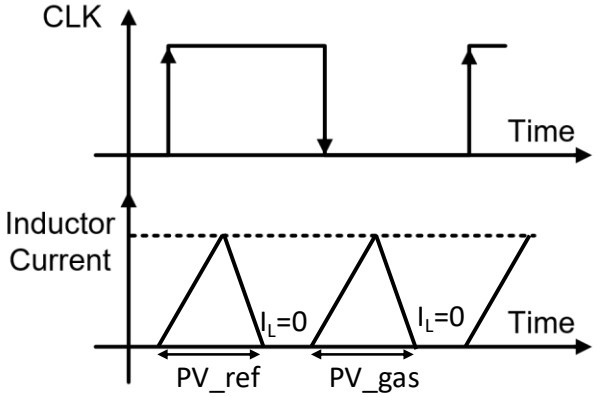

Figure 4.23 Current waveform of Dual-Input Shared-Inductor boost converter

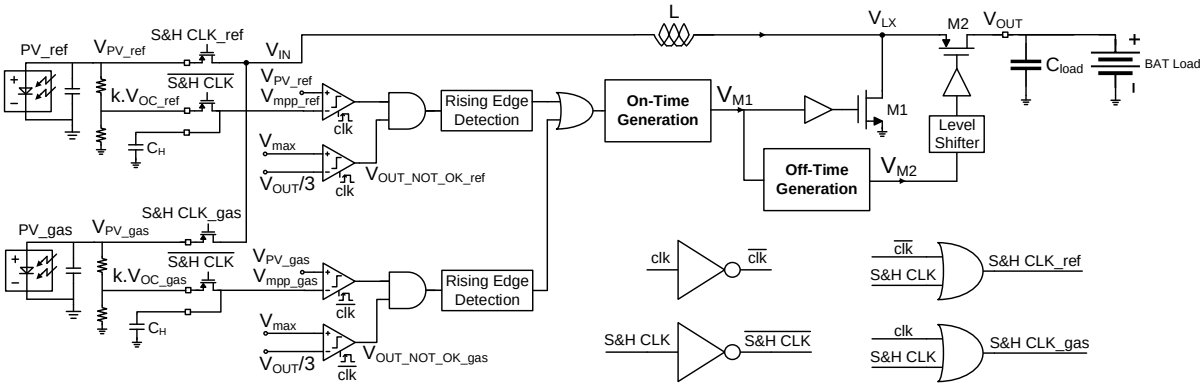

Figure 4.24 Dual-Input Shared-Inductor Boost Control Cituit

The operation of the LED control is simple (Figure 4.25). When $V_{PV} < V_{MIN}$ which means the ambient light is low, the power switch M3 is turned on. Consequently, the LED is on.

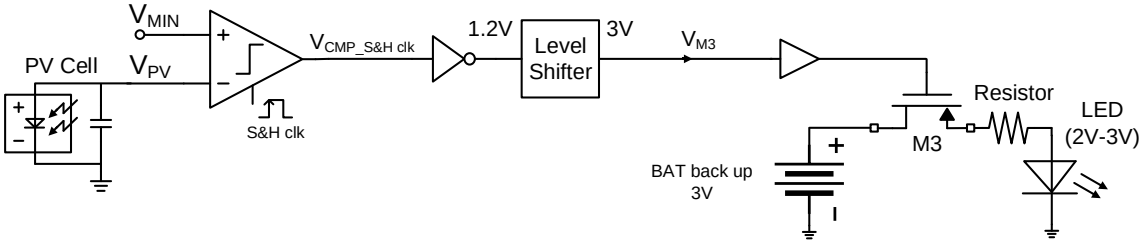

Figure 4.25 LED control diagram

4.4.4 Gas signal Processing

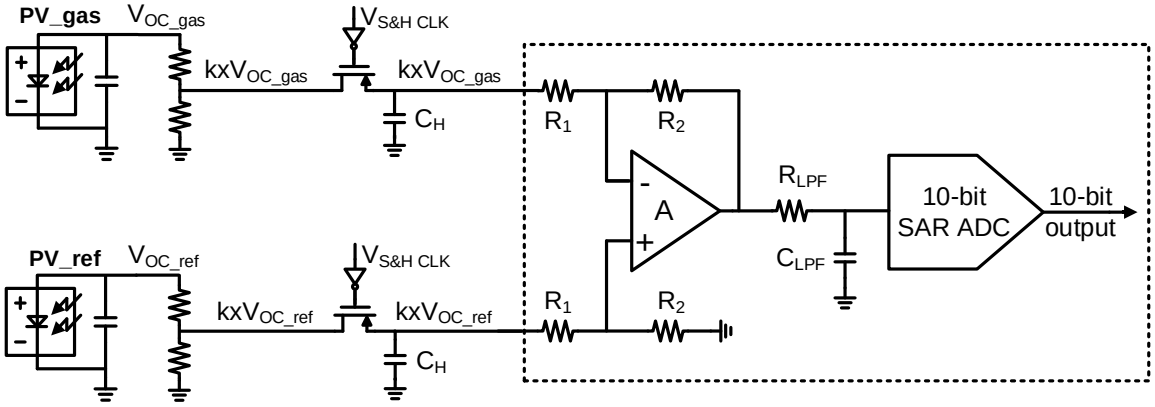

Figure 4.26 Gas signal processing diagram

The gas signal processing block has an opamp voltage subtractor and a 10-bit SAR ADC (Figure 4.26). The opamp subtractor is used to subtract $0.85xV_{OC_ref}$ and $0.85xV_{OC_gas}$ for detecting the voltage change on the PV cells. Because the gas sensing range from 0.2ppm to 200ppm, a 10-bit resolution is needed for the ADC. The SAR ADC is used since it has low power consumption and simple implementation.

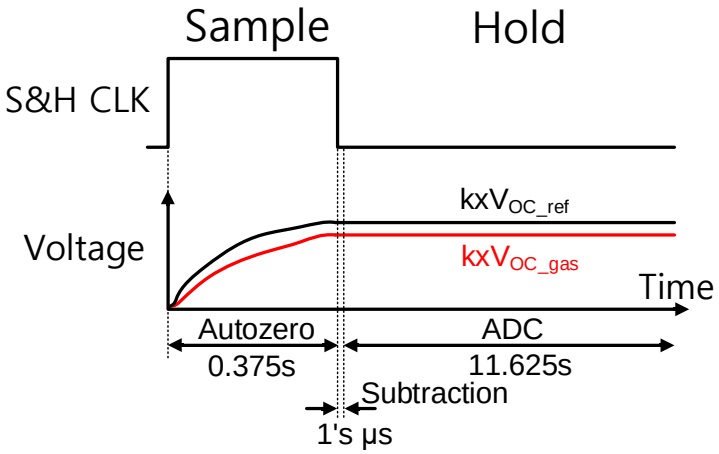

Figure 4.27 Timing operation of the offset cancellation

An input-offset-storage autozeroing technique [10] is used for the opamp offset cancellation as the opamp offset greatly affects the accuracy of gas sensing and the system is discontinuous-time. The timing operation of the offset cancellation is shown in Figure 4.27. During the sample period, the IC will do the offset cancellation. During the hold period, the IC will do the voltage subtraction.

The opamp subtractor with autozeroing offset cancellation circuit is shown in Figure 4.28. During the autozero phase, S1 is on and S2 is off, so V_{OS} is sampled on C_H. During the subtraction phase, S2 is on and S1 is off, so V_{OS} in the positive input is canceled by V_{OS} on C_H. As a result, V_{OS} is compensated.

The residual offset is 0.08mV, and the input referred noise when integrated over the bandwidth of 7.8Hz is 0.046mV rms. The residual offset and the input referred noise are smaller than the detecting resolution (0.43mV).

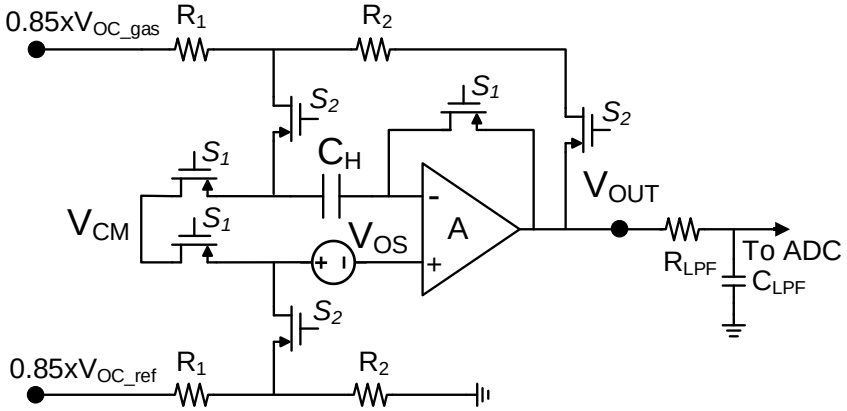

Figure 4.28 Opamp Subtractor with Autozero Offset Cancellation circuit

A two stages opamp (Figure 4.29) is used with the performances, including high gain (63.7dB), low power consumption (912nW), moderate slew rate (0.24V/μs) because the frequency is low.

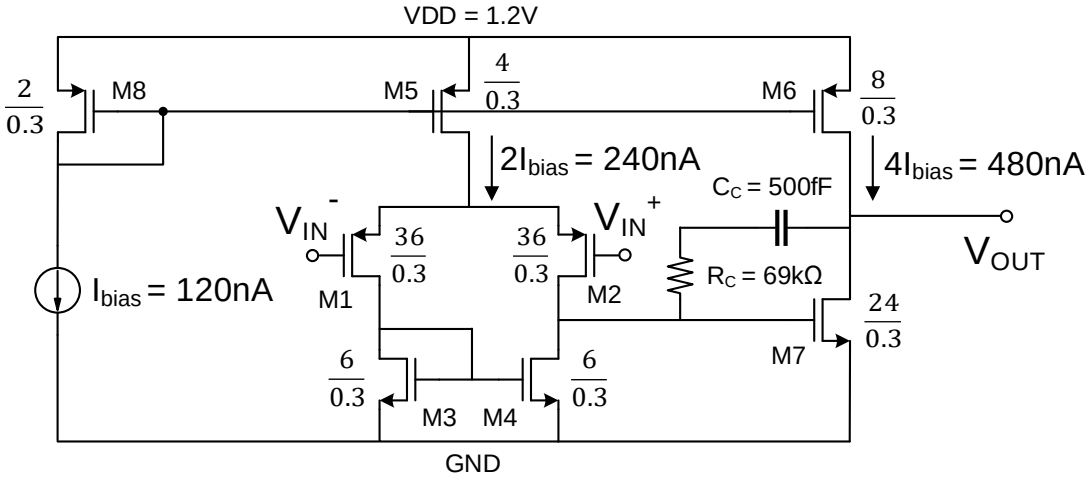

Figure 4.29 Two-stages Opamp circuit

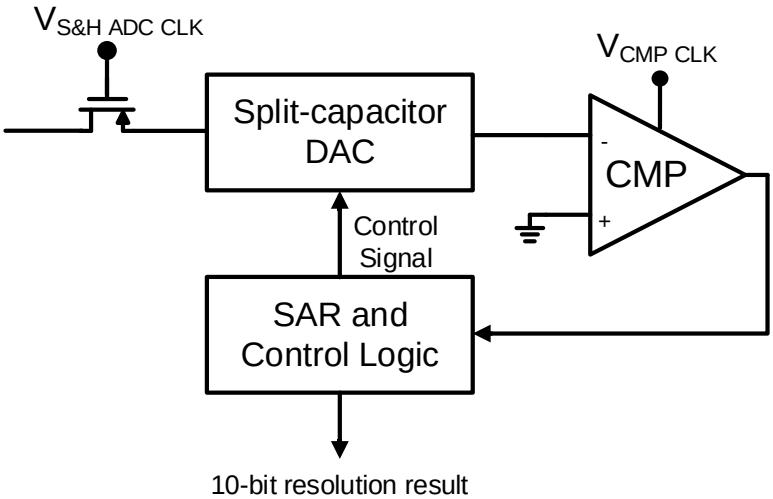

Figure 4.30 10-bit SAR ADC diagram

Because the sampling frequency of the ADC (Figure 4.30) is low, it will achieve low power consumption. Therefore, the design focuses on the input capacitance and the area. In order to achieve a low input capacitance and a small area, a split-capacitor DAC architecture (Figure 4.31) is used. However, the conventional architecture has two disadvantages. Firstly, C_{bri} is difficult to design because it is a fraction of C_u. Secondly, the parasitic capacitors cause gain error and linearity error.

Therefore, a modified architecture [11] (Figure 4.32) is used. C_{bri} is C_u instead of a fractional value of C_u. The last C_u in the LSB array is removed. By doing so, it can improve the matching of C_{bri}. Although it is still vulnerable to the parasitic capacitors and causes 1LSB gain error, the gain error can be easily corrected by digital circuits.

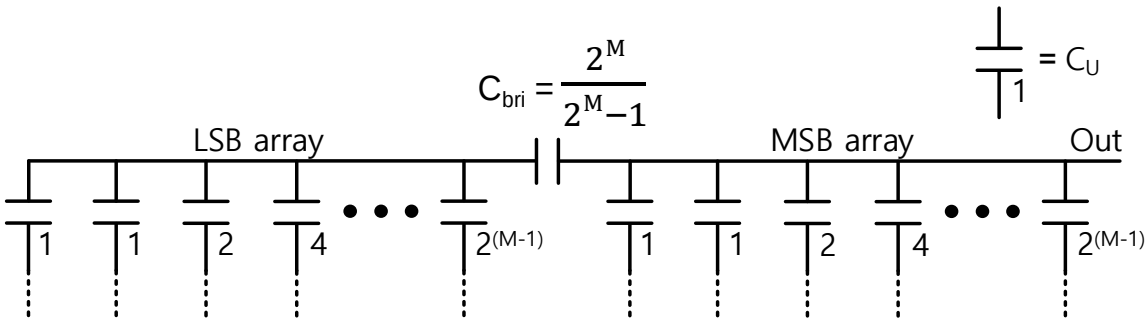

Figure 4.31 Conventional Split-capacitor DAC architecture

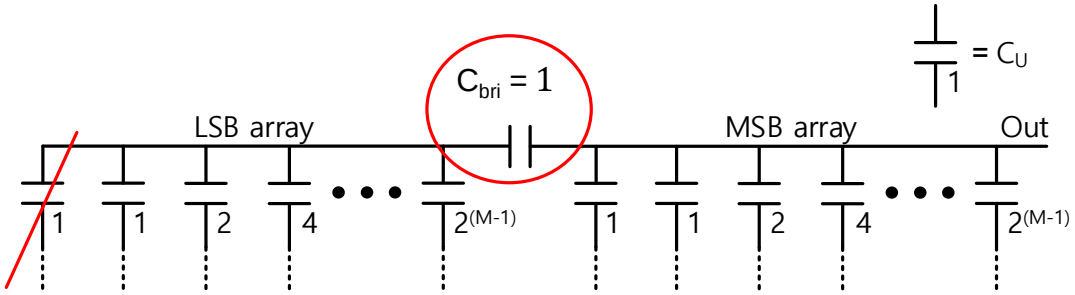

Figure 4.32 Modified bridge solution DAC architecture

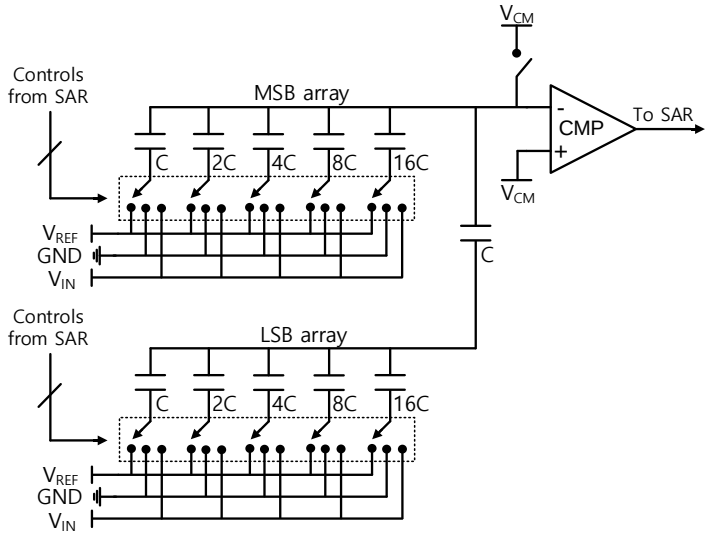

Figure 4.33 Proposed 10-bit Split-cap SAR ADC

The proposed 10 bits split-capacitor ADC is shown in Figure 4.33. The unit capacitor (C) is 133fF.

In the ADC, the comparator offset greatly degrades the ADC performances, so an offset cancellation for the comparator [12] is used (Figure 4.34). The calibration circuit is in the dash circles. It consists of a charge pump and two current sources. Figure 4.35 explains the working principle. During calibration, two inputs of the comparators are connected to the common voltage. Then the voltage on the hold capacitor Vc is tuned to a value at which the offset of the comparator is compensated. Based on the polarity of the offset voltages, Vc will go up or go down. In this case, it goes down. The calibration of the comparator is also done in the sample period of the sample and hold clock, which is similar to the voltage subtractor offset cancellation.

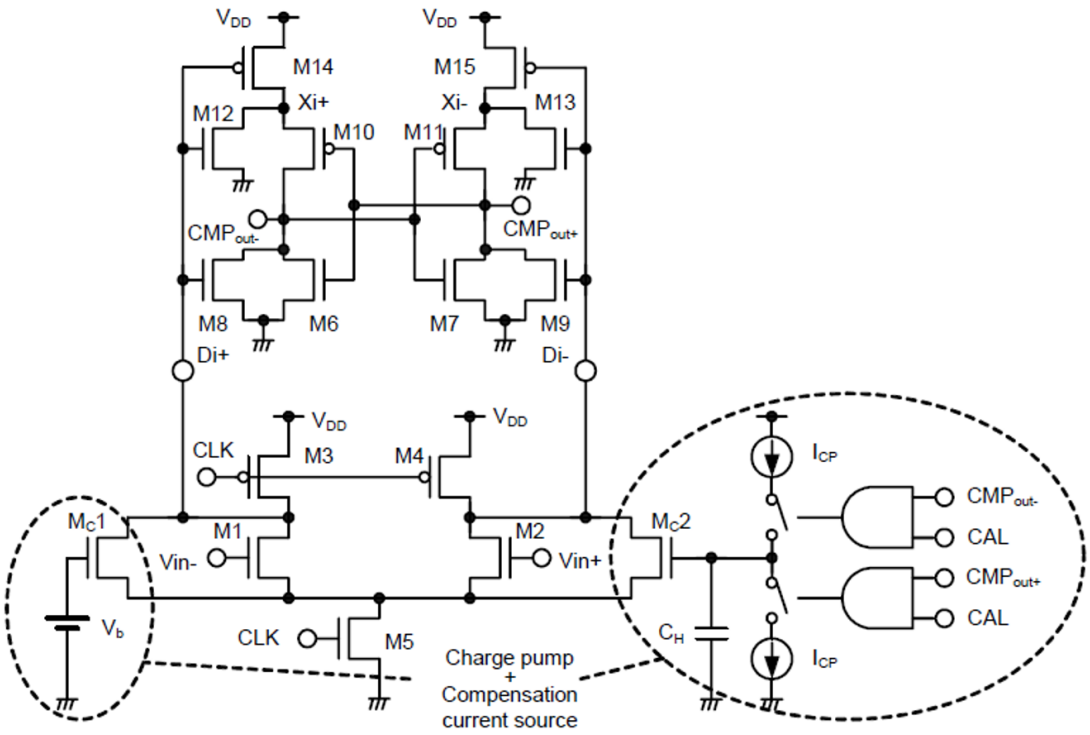

Figure 4.34 Self-calibrating comparator

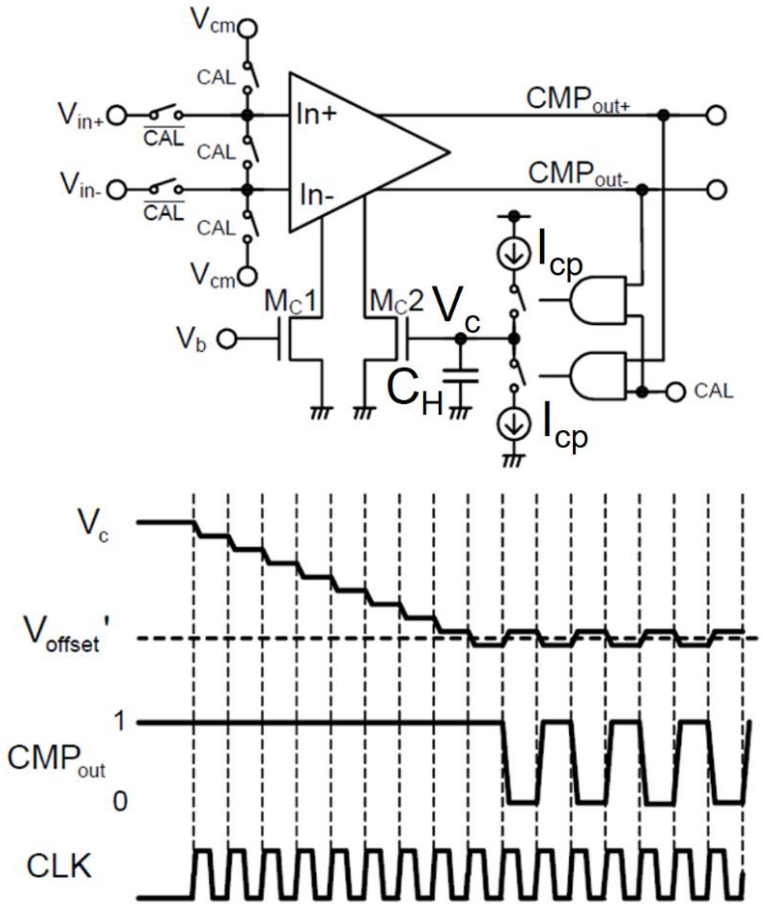

Figure 4.35 Timing operation of the self-calibrating comparator

Chapter 5. Implementation Results and Discussions

5.1 IC Layout

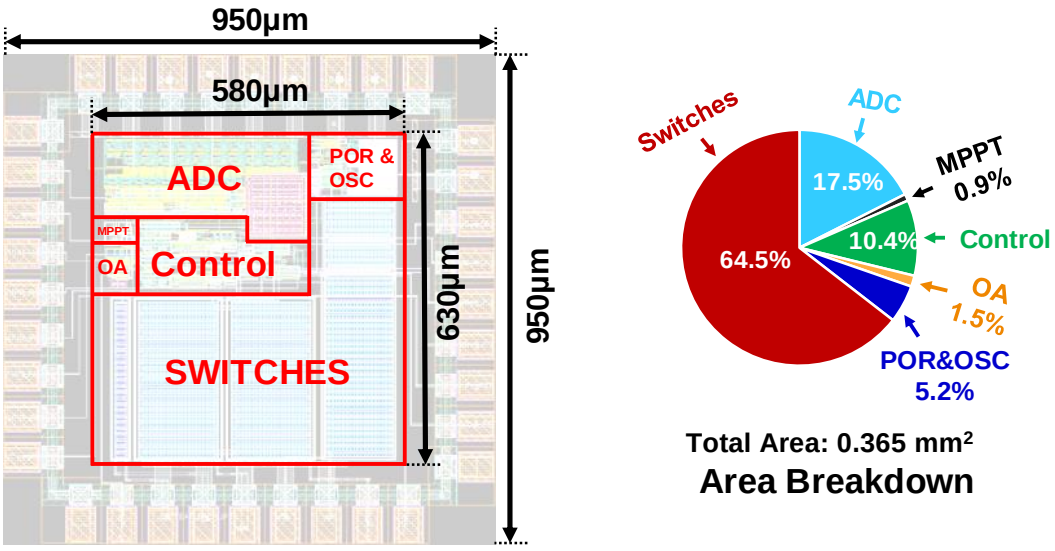

Figure 5.1 IC Layout and Area Breakdown

The IC layout and the area breakdown are shown in Figure 5.1. The chip area is 0.903mm^2, and the active area is 0.365mm^2. The ADC occupies only 17.5% of the active area thanks to the split-capacitor DAC architecture. The most area is occupied by the power switches.

5.2 Energy Harvesting Results (Post-layout)

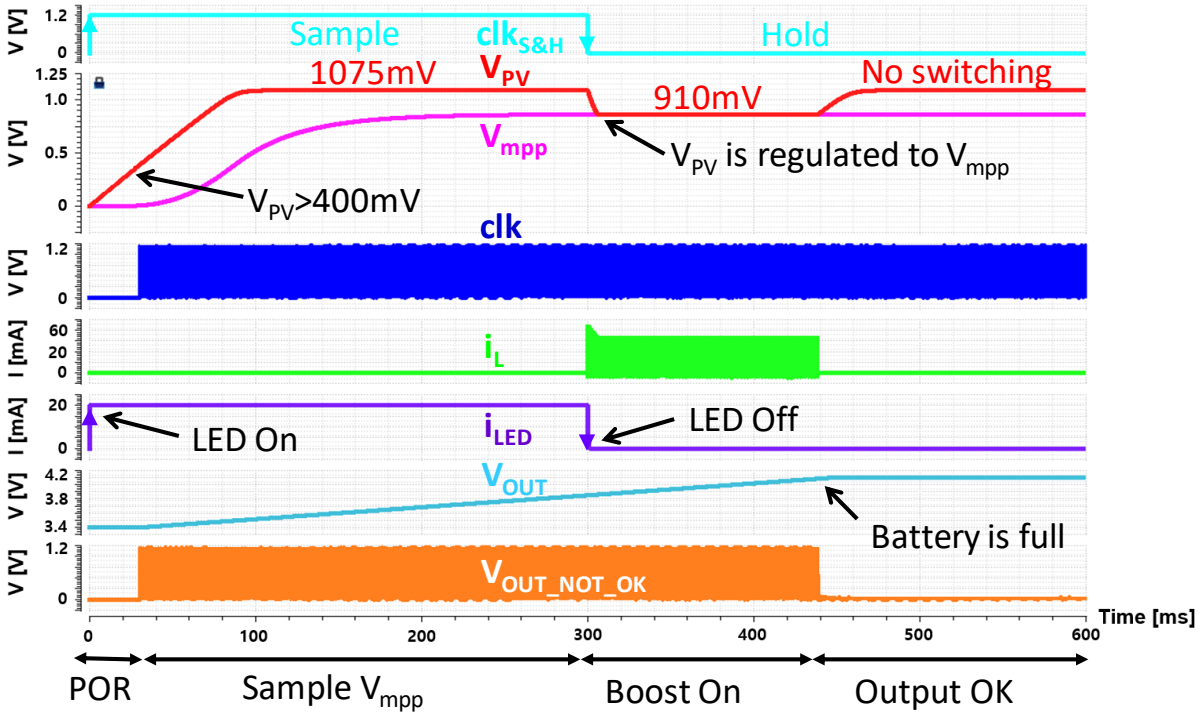

Figure 5.2 Boost and LED Control waveforms

Figure 5.2 shows the boost and LED control waveforms. For simplicity, the waveform of one PV cell is given. In the beginning, the PV cell starts to charge in the input capacitor from 0V to the open circuit voltage (1075mV), and V_{mpp} follows V_{PV}. When V_{PV} goes over 400mV, the POR circuit will turn the enable signal to high. As a result, the oscillator starts creating the clock. When the clock exists, the IC starts sampling V_{mpp}. Because V_{PV} starts from 0V in the beginning, the IC thinks there is not enough light ambient. Therefore, the LED is turned on at the rising edge of $clk_{S\&H}$. Of course, from the next rising edge, the LED is only turned on if there is really not enough light ambient. When $clk_{S\&H}$ goes low, the LED is turned off, and the IC is in the boost mode. The IC starts switching, and the inductor current is built up. Then, V_{PV} is regulated to V_{mpp}. When V_{OUT} approaches the maximum value which means the load battery is full, $V_{OUT_NOT_OK}$ goes low, and the IC stops switching. Therefore, V_{PV} goes up to V_{OC}.

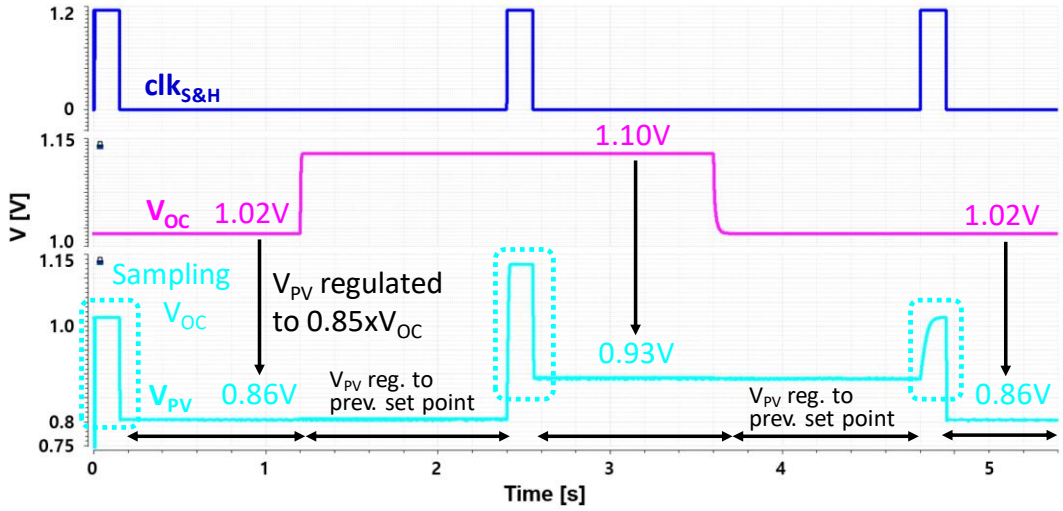

Figure 5.3 MPPT Waveforms

Figure 5.3 demonstrates the MPPT waveforms. If $clk_{S\&H}$ is high, the IC will sample V_{OC}. Therefore, V_{PV} goes up to V_{OC}. When $clk_{S\&H}$ goes low, V_{PV} is regulated to $0.85xV_{OC}$. Although at this point V_{OC} increases, V_{PV} still keeps constant. Similarly, in the next $clk_{S\&H}$ cycle, although V_{OC} decreases, V_{PV} still keeps constant during the hold time. In the third cycle of $clk_{S\&H}$, the operation also remains similar.

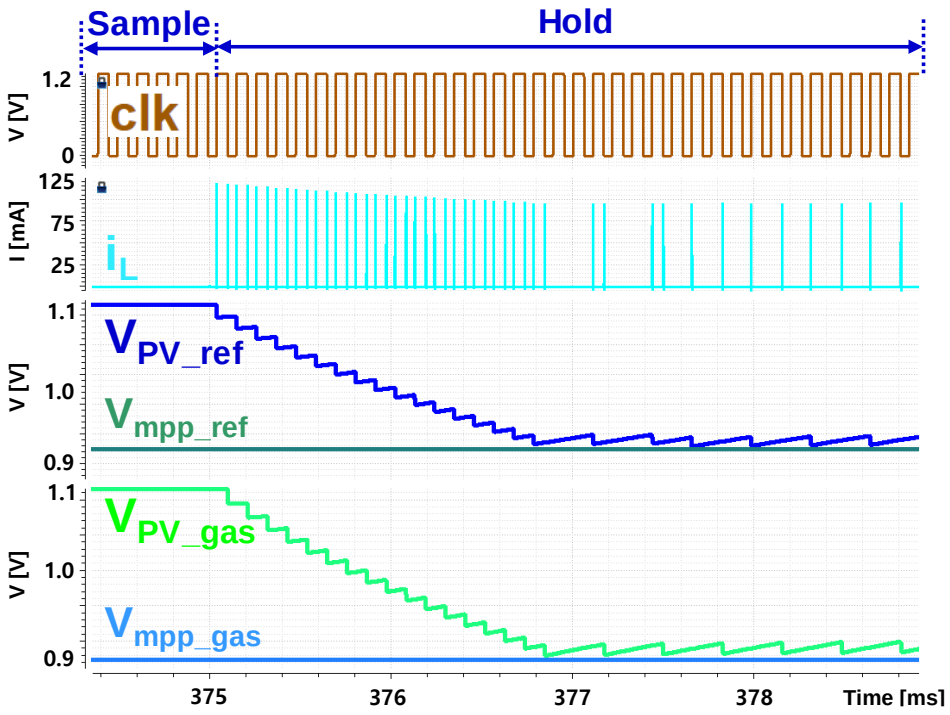

(a)

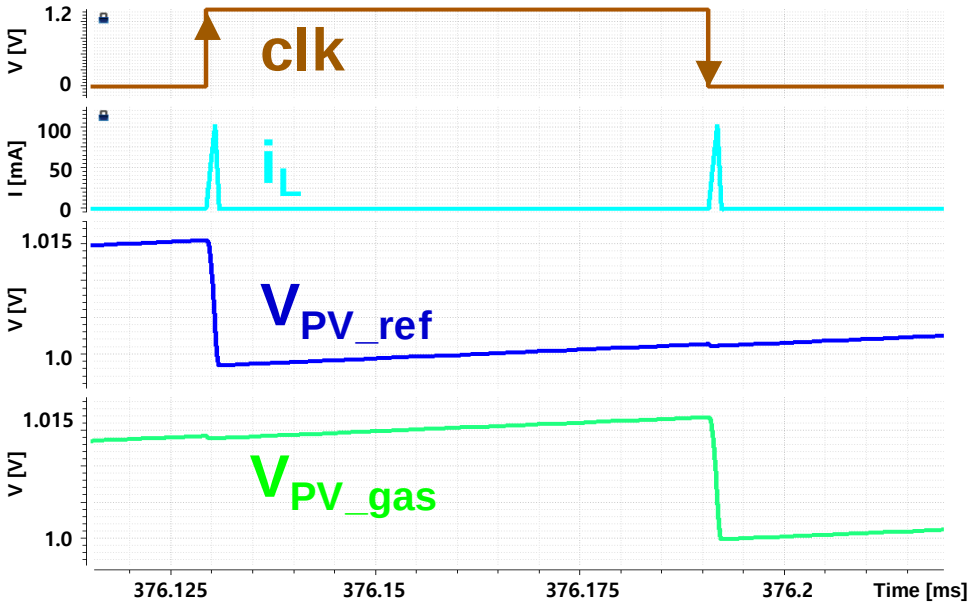

(b)

Figure 5.4 (a) Dual-Input Shared-Inductor waveforms (b) Enlarged view at 376ms

The dual-input shared-inductor waveforms are shown in Figure 5.4 (a). During the sample period, both V_{PV_ref} and V_{PV_gas} are open circuit voltages. During the hold period, the IC regulates V_{PV_ref} and V_{PV_gas} to two different V_{mpp}. A pulse skipping modulation is used as V_{PV} reaches V_{mpp}. In the enlarge view at 10.5ms (Figure 5.4 (b)), the IC regulates V_{PV_ref} at the clk rising edge and V_{PV_gas} at the clk falling edge.

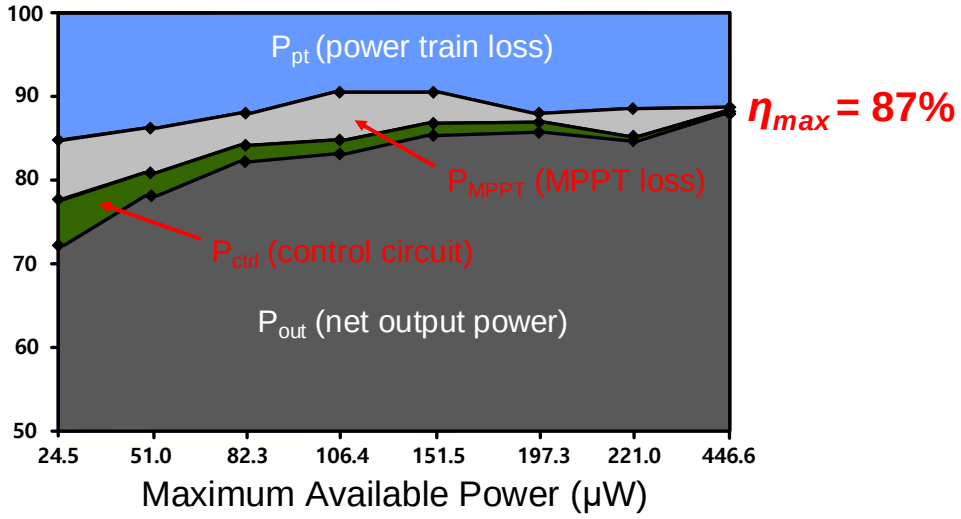

Figure 5.5 Dual-Input Shared-Inductor Boost Converter End-to-End Efficiency

As shown in Figure 5.5, the maximum efficiency is 87% at 446.6μW maximum available power from two PV cells. The power loss almost comes from the power train and the input mismatch.

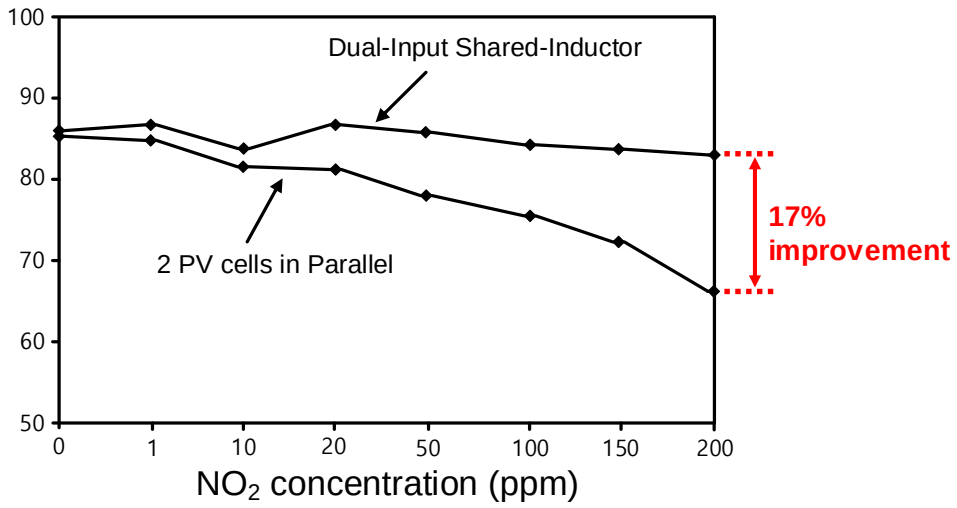

Figure 5.6 End-to-End Efficiency with the different gas concentrations

Figure 5.6 depicts the efficiency with the different gas concentrations. Using dual-input shared-inductor shows 17% improvement of efficiency at 200ppm gas concentration compared to connecting two PV cells in parallel.

Table 5.1 Comparison of Energy Harvesting Converters

	Y.Qui ISSCC'2011	**K. Kadirvel ISSCC'2013**	**Y. Lu ISSCC'2016**	**This work**
Converter Architecture	1 stage, 1 inductor Boost	1 stage, 1 inductor Boost	1 stage, 1 inductor Boost	1 stage, 1 inductor-shared Boost
MPPT mechanism	Constant T_{ON} Fixed F_{SW}	Constant T_{ON} Fixed F_{SW}	Not Reported	Constant T_{ON} Fixed F_{SW}
Quiescent Current	Not Reported	330nA	200nA	**270nA**
Peak Efficiency	70%	80%	85%	**87%**
Application	Battery charger	Battery charger	Battery charger	**Gas sensor system**

Table 5.1 compares this work to the state of the arts boost converters. This work has a comparable quiescent current (270nA) and peak efficiency (87%). However, other works are only for battery charger while this work does both battery charging and gas sensing.

5.3 Gas Signal Processing Results (Post-layout)

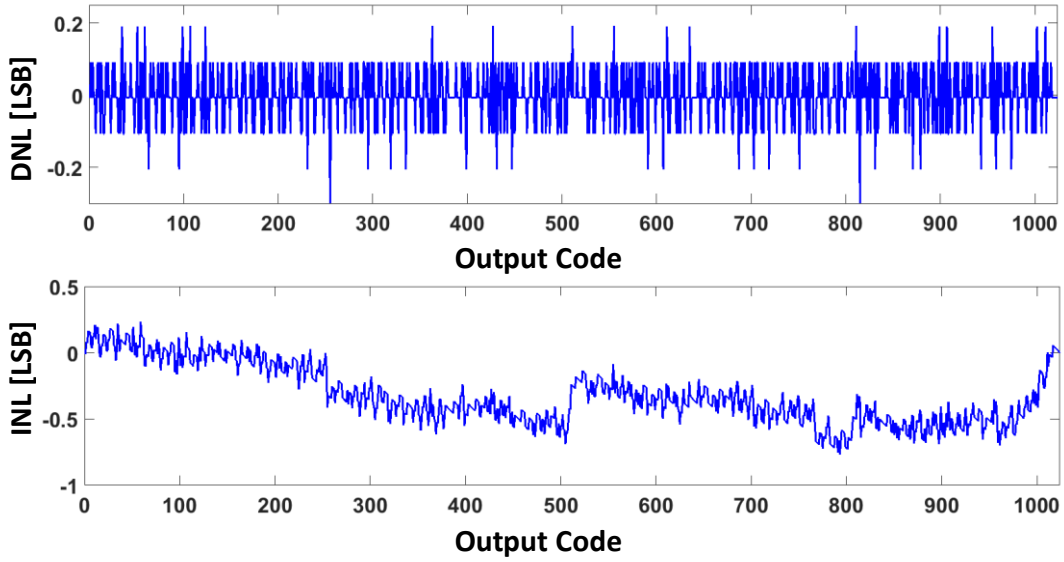

Figure 5.7 10-bit SAR ADC Static Performances

Figure 5.7 shows the ADC static performances with DNL and INL plots. The static performance is quite good with the peak DNL of 0.19/-0.3 LSB and the peak INL of 0.23/-0.76 LSB.

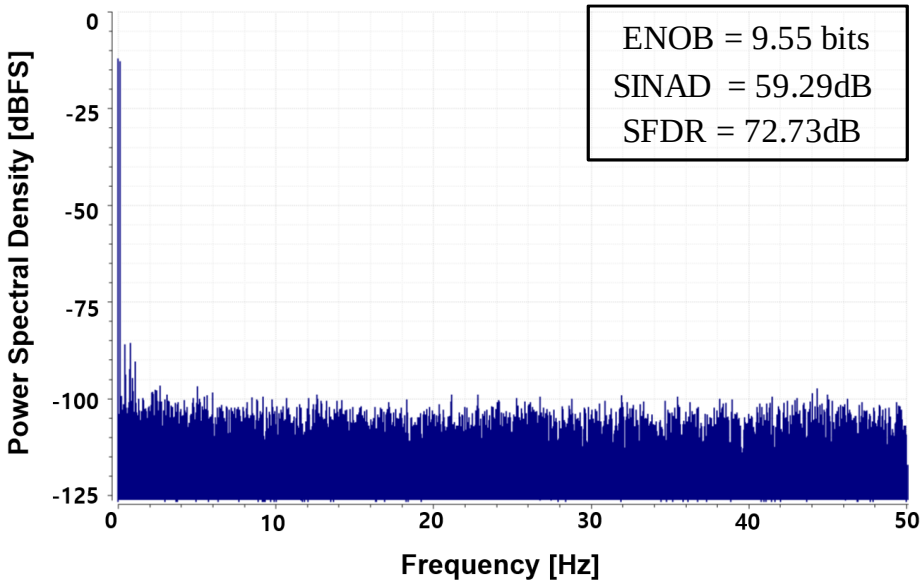

Figure 5.8 10-bit SAR ADC Dynamic Performances

The dynamic performances with the plot of simulated FFT spectrum at 100S/s and 0.158Hz input is shown in Figure 5.8. It shows a high ENOB value of 9.55.

Table 5.2 summarizes the ADC performances. The power consumption is relatively small compared to the remaining parts in the IC. It has low active area thanks to split cap architecture.

Table 5.2 Summary of ADC performances

ADC Architecture	Split-cap SAR
Supply Voltage	1.2V
Input range	120.86mV-1150.5mV
Sampling Rate	100S/s
Resolution	10bits
Power Dissipation	74nW
Peak DNL	0.19/-0.30LSB
Peak INL	0.23/-0.76LSB
ENOB	9.55bits at 0.158Hz
Active Area	0.05mm^2

5.4 Power Breakdown (Post-layout)

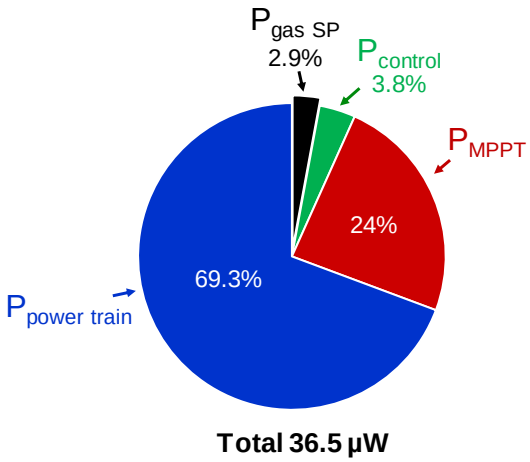

Figure 5.9 Power Breakdown

Figure 5.9 shows the power breakdown at the input power of 221µW. The gas signal processing block has the smallest power consumption with only 2.9% of total IC power consumption, which implies that the IC integrates the gas signal processing into the boost converter with approximately free of power. The most consuming parts are the power train and the MPPT losses.

Chapter 6. Conclusion and Future Work

In this thesis, an IC used for photovoltaic energy harvesting and NO_2 gas sensing is presented. The dual-input inductor-shared boost converter and split-capacitor DAC architecture are used for harvesting power from two PV cells in the case after gas exposure and achieving the small area, respectively. The current IC is most suitable for wireless sensor networks which are used for the analysis of NO_2 in the indoor workplaces.

The IC is implemented by 0.18μm CMOS 1-Poly 6-Metal process. Normally, it operates at the input range from 400mV to 1.1V and at the output voltage of 3V. High peak efficiency of 87% and low quiescent current of 270nA are achieved. Gas sensing interface circuit with on-chip offset calibration has low offset of 500μV, low power consumption of 1.1μW. It also shows high ADC static, dynamic performances (DNL, INL, ENOB) and covers the health care gas detection range from 0.2ppm to 200ppm. Using dual-input shared-inductor boost converter shows efficiency enhancement of 17% at 200ppm NO_2.

The IC will be fabricated to verify its simulated performances with the measurement results. In the future, the IC needs improvements with more sophisticated designs for higher efficiency, lower quiescent current, and higher gas signal processing performances. Furthermore, the IC can be integrated with other sensors, such as temperature and humidity in order to monitor more environmental factors.

References

[1] I. Lee, S-J. Choi, K-M. Park, S. Lee, S. Choi, I-D. Kim, C. Park, "The stability, sensitivity and response transients of ZnO, SnO_2, and WO_3 sensors under acetone, toluene and H_2S environments", *Sens. Actuator B-Chem*., vol. 197, pp. 300-307, 2014.

[2] N-J. Choi, H-K. Lee, S. Moon, W. Yang, J. Kim, "Stacked-type potentiometric solid state CO_2 gas sensor", *Sens. Actuator B-Chem*. vol. 187, pp. 340-346, 2013.

[3] M. Alexy, M. Hanko, S. Rentmeister, J. Heinze, "Disposable optochemical sensor chip for nitrogen dioxide detection based on oxidation N,N′-diphenyl-1,4-phenylenediamine", *Sens. Actuator B-Chem*., vol. 114, pp. 916-927, 2006.

[4] Kyungnam Kang, Kwangmin Na, Donguk Kwon, Jung-Yong Lee, and Inkyu Park, "Self-powered gas sensor using thin-film photovoltaic cell and microstructured colorimetric film", *Transducers*, 2017.

[5] Alireza Khaligh, Omer C. Onar, "Energy harvesting: Solar, Wind, and Ocean Energy Conversion Systems", CRC Press, Taylor & Francis Group, 2010.

[6] Inho Park, Junyoung Maeng, Dongju Lim, Minseob Shim, Junwon Jeong, Chulwoo Kim, "A 4.5-to-16μW Integrated Triboelectric Energy-Harvesting System Based on High-Voltage Dual-Input Buck Converter with MPPT and 70V Maximum Input Voltage", *ISSCC*, 2018.

[7] Yanfeng Lu, Suyi Yao, Bin Shao, Paul Brokaw, "A 200nA Single-Inductor Dual-Input-Triple-Output (DITO) Converter with Two-Stage Charging and Process-Limit Cold-Start Voltage for Photovoltaic and Thermoelectric Energy Harvesting", *ISSCC*, 2016.

[8] Gyuhyeong Cho, "Electronic Circuits For Green Energy", KAIST Lectures.

[9] Yi-Hsiang Wang, Yi-Wei Huang, Peng-Chang Huang, Hsuan-Ju Chen, and Tai-Haur Kuo, "A Single-Inductor Dual-Path Three-Switch Converter With Energy-Recycling Technique for Light Energy Harvesting", *JSSC*, vol. 51, no.11, 2016.

[10] Christian C.Enz, Gabor C. Temes, "Circuit Techniques for Reducing the Effects of Op-Amp Imperfections: Autozeroing, Correlated Double Sampling, and Chopper Stabilization", *Proceeding of the IEEE*, vol. 84, no. 11, 1996.

[11] Andrea Agnes, Edoardo Bonizzoni, Piero Malcovati, Franco Maloberti, "A 9.4-ENOB 1V 3.8μW 100kS/s SAR ADC with Time-Domain Comparator", *ISSCC*, 2008.

[12] Masaya Miyahara, Yusuke Asada, Daehwa Paik, and Akira Matsuzawa, "A Low-Noise Self-Calibrating Dynamic Comparator for High-Speed ADCs", *ASSCC*, 2008.

Acknowledgments

I would like to express my appreciation to all those who helped me during my 2-year Master's degree program.

Firstly, I would like to thank my advisor Prof. Minkyu Je for his help. Prof. Je taught me not only research skills in circuits and systems fields but also presentation skills, problem-solving skills and critical thinking which would be applied in many aspects. In this relatively short period, my graduation owes much to Prof. Je's incites and patience in reviewing my work, answering my questions, and keeping me focused on my goals.

Besides, I would like to thank every member in our lab. In the beginning, they helped me to translate the Korean websites and provided necessary facilities. They also gave a lot of experience, which allows me to adapt to the new environment in Korea. In addition, I received many valuable comments on my work from them in the lab meetings.

Last but not least, I am indebted to my parents, my siblings, and my Vietnamese friends who have been supporting, caring and assisting for me. Their encouragements are my motivation to move forward.

Curriculum Vitae

Name : Hung Phan
Date of Birth: 1994.09.10
Nationality : Vietnam

Education

2012.08-2017.06 Hanoi University of Science and Technology
2017.02-Present KAIST, School of Electrical Engineering